1 2  9 0

UNIVERSIDADE D
COIMBRA

Bruna Cristina Sérgio Lima

Time-gated system for measuring optical parameters of dispersive media

Dissertação no âmbito do Mestrado Integrado em Engenharia Física, ramo de Instrumentação,
orientada pelo Professor Doutor António Miguel Lino Santos Morgado
e apresentada ao Departamento de Física da Faculdade de Ciências e Tecnologia
da Universidade de Coimbra.

Setembro de 2019

UNIVERSIDADE D
COIMBRA

Bruna Cristina Sérgio Lima

TIME-GATED SYSTEM FOR MEASURING OPTICAL PARAMETERS OF DISPERSIVE MEDIA

Dissertação no âmbito do Mestrado Integrado em Engenharia Física, ramo de Instrumentação, orientada pelo Professor Doutor António Miguel Lino Santos Morgado e apresentada ao Departamento de Física da Faculdade de Ciências e Tecnologia da Universidade de Coimbra.

Setembro de 2019

Aos meus pais,

Manuel e Dulce,

OS PILARES DA MINHA PRESERVERANÇA.

Resumo

O objetivo deste projeto foi implementar e testar uma ferramenta capaz de medir as propriedades ópticas de meios turvos, baseada na aproximação de difusão. Esta técnica foi testada a partir de dados adquiridos com um sistema $time-gated$, através de uma geometria de transiluminação. A instrumentação implementada é baseada num díodo laser pulsado e numa câmera intensificada com *gating*. Foi desenvolvida uma ferramenta de ajuste de dados para medir as propriedades ópticas de uma amostra.

Uma superfície de um meio difuso é iluminada com um laser pulsado. Os perfis temporais dos pulsos, emergentes na superfície oposta, são ajustados pela ferramenta desenvolvida, a um modelo teórico que descreve a propagação de luz para meios homogéneos difusos. Realizámos vários estudos com fantomas líquidos e sólidos, baseados em soluções da emulsão lípidica Intralipid. Estes fantomas foram criados de forma a reproduzir as propriedades ópticas de tecidos biológicos e a satisfazer os requisitos inerentes à instrumentação utilizada. Foi medida a função de resposta do instrumento (IRF) do sistema $time-gated$, e esta foi tida em conta pela ferramenta de ajuste de dados experimentais. Em suma, o sistema e a técnica implementados foram capazes de medir o coeficiente de absorção e de dispersão reduzido destes fantomas. A partir dos resultados obtidos, podemos concluir que parece existir um posicionamento para o qual os detectores criados no plano da imagem apresentam um melhor desempenho. No entanto, esta afirmação não pode ser validada sem recorrermos a uma técnica de referência. As medições efectuadas mostram linearidade entre a variação do coeficiente de dispersão reduzido e a concentração de Intralipid presente nos fantomas. É detectado um efeito de redução nas medições do coeficiente de dispersão. Conclui-se que este efeito está

relacionado com a presença de agar nos fantomas, como já tinha sido relatado em estudos publicados.

Palavras-chave: Imagiologia ótica, sistema time-gated, transmitância resolvida no tempo, propagação difusa de luz

Abstract

The goal of this project was to implement and test a diffusion approximation model-based technique capable of extracting the optical properties of turbid media - absorption and reduced scattering coefficients - using data obtained from a time-gated detection system, using a trans-illumination geometry.

We implemented time-gated instrumentation based on a pulsed diode laser and a gated intensified CCD camera and developed a data fitting tool for measuring the optical properties of a slab. The measurement technique is based on the fitting of the temporal profile of the light pulses, acquired at the output of a medium, illuminated on the opposite face with a short laser pulse, with a theoretical light propagation model for homogeneous media. Several studies were performed using liquid and solid phantoms based on solutions of Intralipid fat emulsion, designed to mimic optical properties of biological tissues and to satisfy the requirements inherent to the instrumentation used. The instrument response function (IRF) of the time-gated system was measured and took into account when fitting experimental data.

The implemented system and technique was able to measure the absorption and the reduced scattering coefficient of the tested phantoms. From the results obtained, we can conclude that it seems to exist an optimal positioning of the detectors on the image plane, although this statement cannot be fully confirmed without using a reference technique to validate the accuracy of the technique. The measurements show linearity regarding the variation of the reduced scattering coefficient with the concentration of IL in the phantoms. It also detected an agar-related reduction of the scattering coefficient that was reported in similar published studies.

Keywords: diffusion theory, optical imaging, time-resolved transmittance, tissue-phantoms.

Acronyms

CCD Charged-Coupled Device.

CIBIT Coimbra Institute for Biomedical Imaging and Translational.

DA Diffusion Approximation.

DE Diffusion Equation.

EM Electromagnetic.

FOV Field Of View.

FWHM Full Width at Half Maximim.

HRI High Rate Intensifier.

IBILI Instituto Biomédico de Investigação da Luz e da Imagem.

ICCD Intensified Charged-Coupled Device.

IL Intralipid.

IR Infrared.

IRF Instrument Response Function.

LDH Laser Diode Head.

MCP Microchannel Plate.

NIR Near Infrared.

ROI Region of Interest.

RTE Radiative Transfer Equation.

RTT Radiation Transport Theory.

RWM Random Walk Model.

TCSPC Time-Correlated Single Photon Counting.

USAF United States Air Force.

UV Ultraviolet.

List of Figures

List of Tables

Contents

1

Introduction

1.1 Motivation

The term *light* is used to refer to a wide region of the electromagnetic (EM) spectrum, embracing not only the visible region but also an important region, the *therapeutic window* (600-1300 nm).

This near-infrared window corresponds to the region where light is not strongly absorbed by tissues, reaching its maximum depth of penetration. This light can used by non-invasive techniques such as Diffuse Optical Imaging techniques, which have the capabilty of measuring the optical properties of tissues, relying on the monitorization of their spatial-temporal variations.

Consequently, by allowing us to image regional variations of optical properties (for example, oxy- and deoxy-hemoglobin concentration and cellular scattering), we can create spatial maps of tissue properties (hemoglobin concentration, blood oxygen saturation, scattering, etc.).

The mapping of the optical properties is done through model-based reconstruction algorithms and it can be used in many diagnostic and therapeutic applications, such as breast cancer imaging, brain functional imaging, stroke detection, photodynamic therapy, and radiation therapy monitoring.

Hence, the study of the optical properties of tissues is relevant to extract information of tissues and to develop devices, diagnostic measurements and therapeutic protocols by understanding light distribution and energy deposition.

1.2 Context

This work was carried out as part of a new research line of the Instrumentation Group of CIBIT[1], in the field of optical imaging in diffuse media. The creation of the Instrumentation Group took place in the former IBILI[2], in 1994. Since then, the research work has been made through instrumentation development and study methods on ocular morphology and function, which allow it to gain extensive experience in imaging transparent poorly dispersive biological tissues.

In 2018, research work started on imaging diffuse biological media. This new line of research implies a period of scientific and technical learning, once dispersive imaging faces challenges that are not experienced when imaging transparent media.

Naturally, the initial activities in this new line of research focused on the evaluation of techniques to measure the optical properties of diffuse media (namely the absorption and diffusion coefficients), and to produce images of the internal structure of these media using these optical properties as a contrast mechanism.

Hence, three evaluation projects were proposed by the Instrumentation Group: two related to the determination of optical properties of homogeneous media (the first based on time-gated techniques and the second based on optical coherence tomography) and one related to the evaluation of a software suite for image reconstruction in diffuse optical tomography in heterogeneous media.

The approach chosen by the Instrumentation Group was to use and evaluate imaging and optical measurement techniques already used in previous research works.

This dissertation emerges as the beginning of the first-mentioned project, which aims to determine the optical properties of homogeneous media based on a time-gated detection system. This work resorted to the existing instrumentation in the group, to work on a new problem based on samples that the group had never worked with. This circumstance should be taken into account, and it contributes to the initial character of the results presented here.

[1] Coimbra Institute for Biomedical Imaging and Translational
[2] Instituto Biomédico de Investigação da Luz e da Imagem

1.3 Objectives

The main focus of this project was to implement and evaluate the performance of a time-resolved technique capable of extracting the optical properties of turbid media such as the absorption and reduced scattering coefficients.

It was aimmed to test this diffusion approximation model-based technique using data obtained from a time-gated detection system, using a trans-illumination geometry.

To accomplish this goal, it was necessary to define intermediate objectives such as to study the ability to produce phantoms with controllable optical properties and to study the possibility of using an intensified time-gated camera as a detector.

To evaluate of the performance of this technique, it was studied:

- The best location and geometry of the detectors created in the field of view of the camera;
- The linearity of the measurements regarding the variation of the reduced scattering coefficient with the concentration of IL in the phantoms;
- The influence of the presence of agar in phantoms.

1.4 Document Structure

This dissertation begins with a theoretical framework, consisting of the first five chapters. First, in chapter 2, is made a brief approach to the fundamental photophysical processes, from which optical parameters of tissues are obtained.

Then, the optical parameters of tissues and spectral properties of their components are presented in chapter 3, followed by a description of light propagation models.

To end this theoretical framework, chapter 5 provides a review of time-resolved studies based on the referred light propagation models.

Chapter 6 presents the methodology used in this project, addressing the implemented time-resolved experimental set-up, the phantom studies performed and the software description. In chapter 7, the results of the performed

experiments are presented and discussed.

Finally, the conclusions are presented in chapter 8. In Appendix A, the noise model applied to the experimental data is presented.

2

Fundamental Optical Properties

This section discusses the processes that affect light propagation in tissues: refraction, scattering and absorption. The fundamental parameters related to these processes will be briefly explained in the following subsections.

2.1 Refraction

When an electromagnetic wave, such as light, enters a different medium its speed of propagation changes, but not its frequency. Therefore, when light enters a new medium it can be noticed a change in its wavelength, causing the wave to change its direction of propagation. This phenomenon is called refraction.

To fully understand refraction we must be aware of a new concept, the index of refraction, that correlates the speed of light in vacuum with the speed of light in a medium.

The index of refraction, n(λ), determines how light propagates at media boundaries and how the speed of light varies when entering a new medium, as it can be observed in Figure 1. The refractive index depends on the wavelength and is defined as:

$$n\left(\lambda\right) = \frac{c}{c_m\left(\lambda\right)} \tag{2.1}$$

Where $c = 2{,}998 \times 10^8$ m/s represents the speed of light in vacuum, and c_m represents the speed of light in the medium.

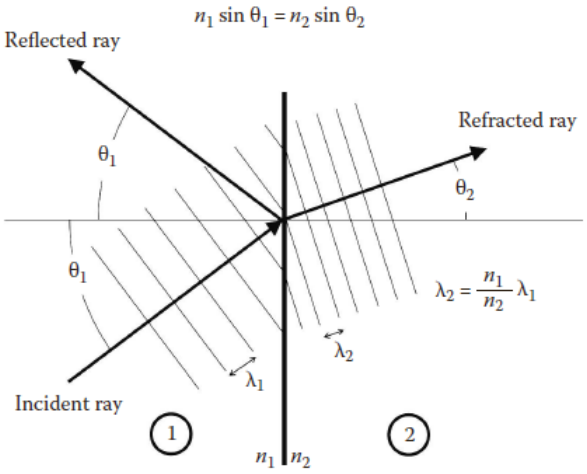

Figure 2.1: Refraction of a incident ray of light in a planar boundary (adapted from [1]).

Consider a boundary between two different media that is crossed by a beam of light. The relationship between the angles of incidence and refraction of the incoming and refracted wave is given by Snell's Law:

$$sin\theta_1 = \frac{n_1}{n_2} \times \sin\theta_2 \tag{2.2}$$

Where n_1 and n_2 are the refractive indices of the two media.

The amount of energy transmitted across or reflected from the boundary is also determined by the refractive indices. Considering only normal incidence ($\theta_1 = 0$), the fraction of the incident energy that is transmitted ($\theta_2 = 0$) into the second medium is given by:

$$T = \frac{4n_1n_2}{(n_1 + n_2)^2} \tag{2.3}$$

The fraction of the incident energy that gets reflected, is also known as Fresnel reflection, and is described as:

$$R = 1 - T = \frac{(n_1 - n_2)^2}{(n_1 + n_2)^2} \tag{2.4}$$

2.2 Scattering

When light finds a local variation of the refractive index of the medium (i.e. a scatterer), scattering occurs and a fraction of its intensity is redirected over a range of angles, as illustrated in Figure 2.2.

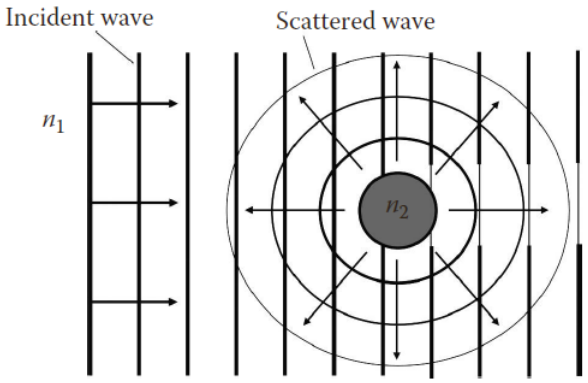

Figure 2.2: Schematic diagram of light scattering from a particle with refractive index n_1, embedded in a medium with refractive index n_2 (adapted from [1]).

Scattering cross section quantifies the scattering properties. A light wave carries energy that is described in terms of intensity of the incident light wave and the amount of power that is scattered. The scattering cross section is given by the ratio between the scattered power and the intensity of the plane wave. It has the dimensions of an area:

$$\sigma_s(\widehat{s}) = \frac{P_{scatt}}{I_0} \tag{2.5}$$

Where $\widehat{s}$ defines the direction of propagation of the plane wave relative to the scatterer. Conceptually, the scattering cross section can be seen as the transverse area that the scatterer should have to remove from the plane wave, an amount of power equal to the observed scattered power.

The scattering coefficient characterizes a medium in which identical scatterers present an uniform distribution, representing the combined cross-sectional area for inclusions per volume. This coefficient is defined as the number of scattering events per unit length and is correlated with ρ, which represents the density of scatterers.

$$\mu_s = \rho\sigma_s \tag{2.6}$$

The scattering mean free path is the distance over which incident light gets reduced to $\frac{1}{e}$ (approximately 37%) of its initial intensity and is given by:

$$l_s = \frac{I}{\sigma_s} \tag{2.7}$$

It represents the average distance a photon travels between consecutive scattering events.

The scattering of an electromagnetic (EM) wave by a homogeneous sphere is described by the Mie solution to Maxwell's equation.

The light scattering theory can be categorized in terms of two frameworks [2]:

- The theory of Rayleigh scattering, which is an approximation that describes scattering by a "small, dielectric (non-absorbing), spherical particles [2];
- The Mie scattering theory, which does not present a particular bound on particle size, encompassing the general solution for the spherical scattering.

By having no size limitations, Mie theory can describe most spherical scattering systems (absorbing and non-absorbing), including Rayleigh scattering. This theory converges to the limit of geometric optics for cases where the scatterers are large particles. Hence, we can identify three different types of scattering, accordingly to the scatterer dimensions:

- Rayleigh limit - where the scatterer dimensions are smaller than wavelength dimensions;
- Mie Regime - where the scatterer dimensions are similar to the wavelength dimensions;
- Geometric Limit - where the scatterer dimensions are much larger than the wavelength dimensions.

2.2.1 Anisotropy

When light scatters off a particular scatterer, the light generally emerges in a preferential direction, relative to its incident angle, as shown in Figure 2.3.

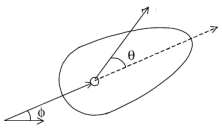

Figure 2.3: The angle of a scatter orientation - ϕ - and the angle of the scattered light - Θ. (adapted from [3]).

The scattering phase function - p(Θ) - describes the angular dependence of scattering and is a function of the angle between the incident and scattered light Θ. It can be interpreted as the probability density function defined along polar angles. This function depends on the relative size of the scattering particle and wavelength of light [4], but is independent of ϕ - the orientation of the scatterer [3].

Photons are deflected in different trajectories when scattered. On average, there is a deflection angle and the mean value of $cos\,(\Theta)$ is defined as the anisotropy factor (g) [dimensionless]. It describes the amount of forward scattering (red arrow in the following figure) retained after the scattering event, expressed as:

$$g = \langle cos\,(\Theta) \rangle \tag{2.8}$$

Figure 2.4, illustrates the concept of anisotropy (g) along with the concept of scattering phase function, p(Θ).

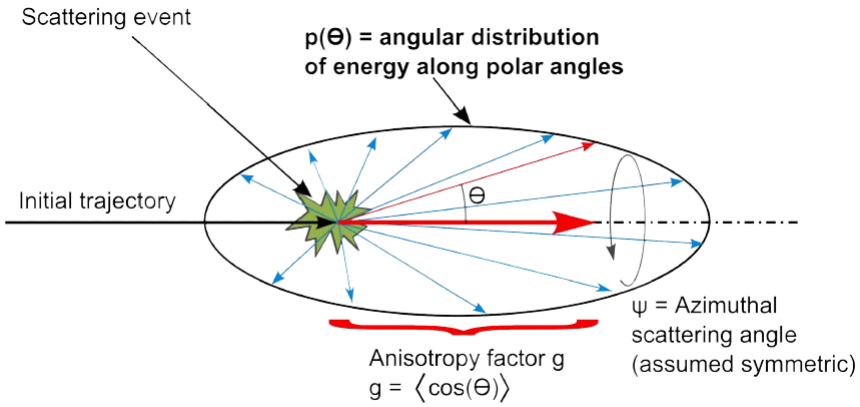

Figure 2.4: The scattering phase function (adapted from [4]).

The anisotropy factor assumes values between -1 and 1.

- g = -1 corresponds to backward scattering, where light is deflected back to the direction from which it came;
- g = 0 corresponds to isotropic scattering, where light is deflected with equal efficiency into all possible directions;
- g = 1 corresponds to forward scattering, where light is deflected in the direction of propagation of the incident light.

The scattering properties of bulk media are often described in terms of the reduced scattering coefficient, $\mu_s^{'}$ which allows us to simplify directional effects [4]. The reduced scattering coefficient can be expressed as:

$$\mu_s^{'} = \mu_s(1 - g) \tag{2.9}$$

2.3 Absorption

The absorption of EM radiation is the process in which molecular or atomic species take up energy from photons, which is being transformed into matter's internal energy. These processes play a significant role in diagnostics applications.

A molecules absorption spectrum can be interpreted as its "fingerprint" for diagnostic and therapeutic applications, as absorption of light energy can produce physical and chemical effects in tissues for treatment purposes. [1].

Absorption processes involve an important concept, energy level, which is a quantum state of an atom or molecule. A transition is the shift of an energy state to another,which can occur in two ways:

- From a lower to a higher energy level, involving absorption of the photon energy equal to the difference in energy, $E_{ph} = \Delta E$, between two levels:

$$\frac{hc}{\lambda} = E_{final} - E_{initial} \tag{2.10}$$

- From a higher energy level to a lower level, a decay which is accompanied by a release of energy equal to the energy difference between two levels. The release of energy may occur with or without emission of photons.

2.3.1 Absorption Cross Section and Coefficient

The absorption cross section - σ_a - can be defined in the same manner as for scattering,

$$\sigma_a = \frac{P_{abs}}{I_0} \tag{2.11}$$

where P_{abs} is the amount of power absorbed out of an initially uniform plane wave of intensity I_0. The absorption cross section is independent of the relative orientation of the incident light and the absorber.

A medium with uniform distribution of identical absorbing particles can be characterized by the absorption coefficient - μ_a - which is defined as the number of absorption events per unit length:

$$\mu_a = \rho\sigma_a \tag{2.12}$$

where ρ is the density of absorbers (number of absorbers per unit of volume).

The absorption coefficient is the inverse of the average distance between successive absorption events.

3

Tissue Properties

As stated by *S. L. Jacques*, "the optical properties of tissues should be regarded as variable from tissue to tissue, person to person and even time to time." [5]
Biological tissues can be described as optically inhomogeneous and as absorbing media [6]. The following section will provide some background on optical properties of tissues and tissue constituents, mentioning some of their typical values.

3.1 Refractive Index

Given the heterogeneity in the composition of biological tissues, scattering properties, like reflection and transmission at boundaries, are calculated using the refractive indexes for the various tissue constituents.

Water constitutes a significant portion of most tissues, which sets the minimum values of n for biofluids and soft-tissue constituents. Melanin particles are a type of soft-tissue component found mostly in the epidermial layer of the skin. These are at the high end of the index scale [6], presented in Table 3.1 .

Medium	n
Water	1.33
Extracellular Fluids	1.36-1.38
Intracellular Cytoplasm	1.36-1.38
Whole Tissues	1.36-1.40
Fatty Tissues	~ 1.45
Melanin Particles	>1.6
Tooth Enamel	1.62-1.73

Table 3.1: Refractive indices of various tissues and tissues components, adapted from [6]

3.2 Scattering Properties

When light encounters a local inclusion with a different refractive index, scattering occurs. In biological tissues, scattering is often the dominant mechanism affecting light propagation. Hence, a very short pulse of collimated light can quickly disperse and become diffuse in a fraction of a millimeter, which caracterizes such tissues as turbid and light diffusers. The diffuse light concept is considered central in tissue optics. Diffusion describes a process in which a member of a group of objects moves in random steps independently of the others [6].

Scattering processes have multiple medical applications. Since these processes depend on the structure and morphology of the tissue components, scattering properties can be modified by abnormalities or diseases, and thus, be useful for diagnostic purposes. Scattering signals may also provide valuable information to therapeutic applications.

A common scattering source in biological tissues is the discrepancy between refractive indices of cellular organelles and the envolving cytoplasm. Thus, subcellular organelles are important scatterers, which typically have sizes larger than the wavelength range of interest. Scattering processes that stream from these cases fall in the Mie regime and exhibit forward-directed scattering patterns that are highly anisotropic [1].

The size and shape of human cells depend on the type of tissue they belong to. Their size can vary from 4 to 100 μm, but typically assumes a size of 10 μm. An

isolated cell can be a strong scatterer, but within a tissue, the scattering is mainly subcellular.[1].

In skin, melanosomes are important scattering structures. They contain melanin particles that are arranged as beads. In blood, the disk shaped erythocytes are the strongest scatterers and so blood scattering properties depend on the hematocrit and the red cell agglomeration. [6]

Scattering in support tissues, formed by cells and extracellular proteins, arises from both the small-scales inhomogeneities and the large-scale variations. Therefore, scattering in support tissues is considered as Rayleigh scattering.

3.2.1 Absorption Properties

The absorption properties of a tissue dictate the capability of light to penetrate the referred tissue. Thus, the region of the EM spectrum where tissues absorption is weak enough to allow light penetration is very important. This region is designated by *therapeutical window* and includes wavelengths from the red region to the NIR (600 to 1300 nm) and demonstrated in Figure 3.1.

At the red region end of the window, absorption occurs mainly by the oxygenated and desoxygenated hemoglobin. There is an increase of approximately two orders of magnitude of the oxygenated hemoglobin absorption as the wavelength shortens in the region of the spectrum around 600 nm.

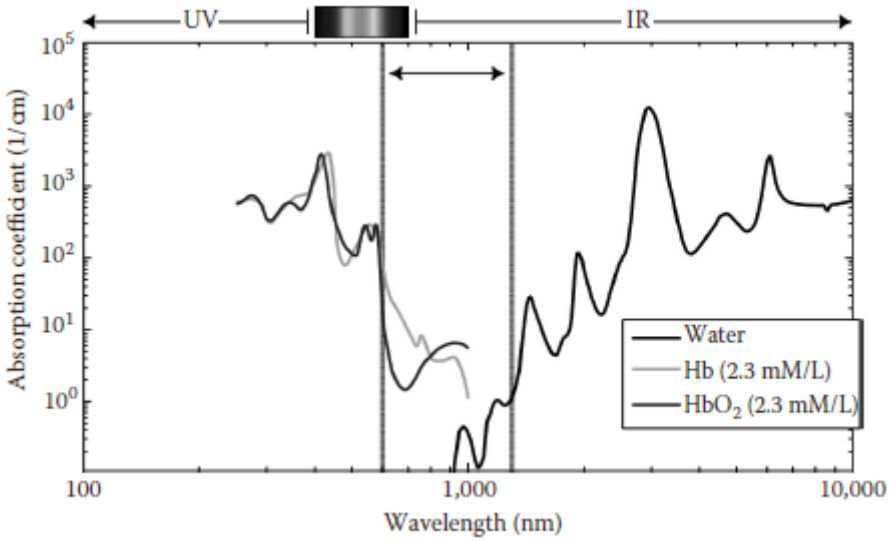

Figure 3.1: The therapeutic window and the absorption spectra of water, oxygenated hemoglobin and oxygenated hemoglobin. From [1].

Within this window, scattering is dominant over absorption, and the penetrating light can become diffuse.

3.2.2 Absorption Properties of Tissue Components

Absorption in tissues is determined by the molecular composition of the tissue. In NIR, water, fat, and hemoglobin are the main contributors towards absorption. The function of a given tissue affects the concentration of oxygenated and desoxygenated hemoglobin. Thus, the analisys of absorption can provide clinically useful physiological information. [7]. The absorbed light can be converted into heat or flurescence radiation, and also being consumed in photobiological reactions. The absorption spectrum depends on the type of predominant absorption centers and on the water content of tissues. Absolute values of absorption coefficients for typical tissues lie in the range of 10^{-2} cm^{-1}.

In infrared (IR) $\lambda \geq 2$ μm spectral regions, light is readily absorbed by water, which accounts for the small contribution of scattering and inability of radiation to penetrate deep into tissues. Short-wave visible light waves penetrate typical tissues as deep as 0.5-2.5 mm, whereupon it undergoes an exponencial decrease in intensity.

3.2.3 Spectral properties of tissue constituents

The values of μ_a and $\mu_s{}'$ of a tissue are in fact its average properties. Biological tissues have many constituents, each of which affect light propagation. For instance, absorption and scatter properties are influenced by the oxygenation state of blood in the tissue [3].

Figure 3.2 shows the absorption spectrum of common tissue constituents highlighting the NIR region, in which hemoglobin exhibits higher absorption properties when compared to water.

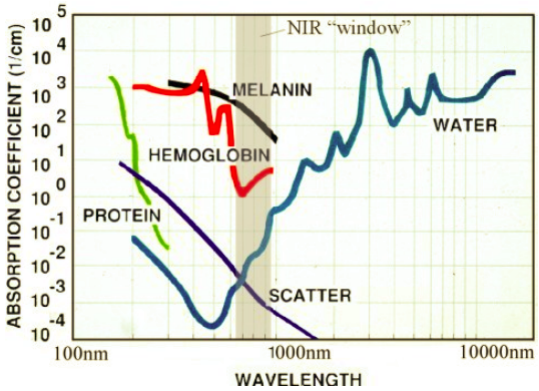

Figure 3.2: General tissue constituents and their absorption spectrum. Adapted from [3]

In the following sections we will discuss the spectral properties of important chromophores in biological tissues. Since scattering shows a weak dependence on wavelength, the NIR window is essentially limited by light absorption.

3.2.3.1 Water

Given the high concentration of water in biological tissues, it is of high importance to fully understand its behavior through the spectrum, in terms of absorption and scattering. The absorption spectrum of water is presented in Figure **??** in the range from 100 to 10000 nm.

In the range of visible light, water is almost transparent, although in the NIR it assumes an absorbing behavior. From this figure we can infer that water absorption assumes low values. Even so it contributes to the overall absorption of tissues.

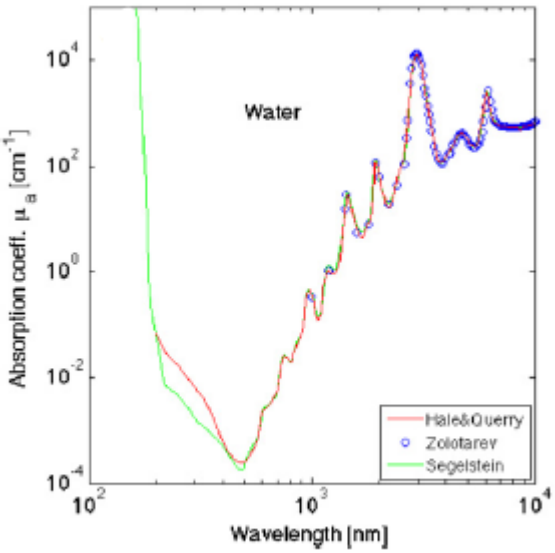

Figure 3.3: Absorption coefficient of water versus wavelength. Adapted from [5]

3.2.3.2 Hemoglobin

There are two main types of hemoglobin: oxyhemoglobin (where the hemoglobin molecule is bounded to oxygen) and deoxyhemoglobin (where the hemoglobin molecule is free).

Each one of these types of hemoglobin exhibits a different absorption spectra that is normally represented in terms of molar extinction coefficients, as shown in Figure **??**. Molar extinction coefficient measure how strongly a substance absorbs light at a given wavelength, per molar concentration.

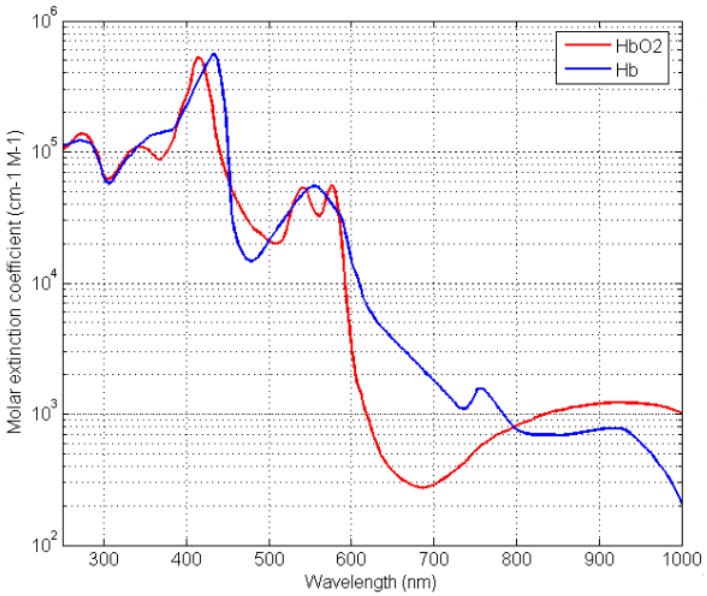

Figure 3.4: Molar extinction coefficients of oxy and deoxyhemoglobin, from [8].

The highest absorption peaks of molar coefficients are at 420 nm for deoxyhemoglobin and at 410 nm for oxyhemoglobin. Deoxyhemoglobin has a second peak at 580 nm, decreasing for higher wavelengths and oxyhemoglobin shows two secundary peaks, at 550 e 600 nm, decaying much faster than deoxyhemoglobin. The points with equal molar extinction coefficient for deoxyhemoglobin and oxyhemoglobin are called isosbestic points.

3.2.4 Melanin

Melanin is a chromophore that exists in the human epidermal layer of skin and it is considered as a protective agent against harmful UV (ultraviolet) radiation. It is one of the major light absorbers in biological tissues, although it presents a smaller contribution than other constituents.

There are two main types of melanin: eumelanin and pheomelanin. The molar extinction coefficient spectra of both types and its wavelength dependence are represented in Figure 10, expressed in $[(\text{cm})^{-1}\ (\text{moles/liter})^{-1}]$.

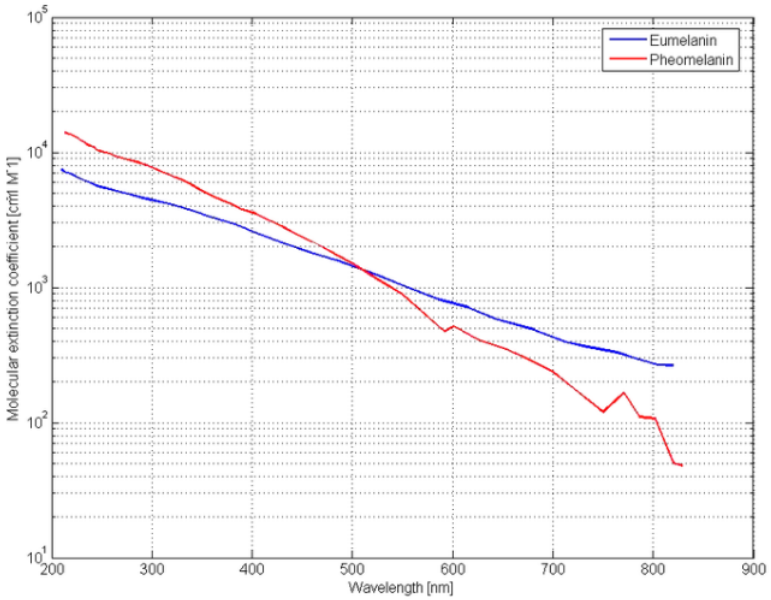

Figure 3.5: Molar extinction coefficient *vs.* wavelength for eumelanin monomers and pheomelanin monomers, from [9].

3.2.5 Fat

One of the major tissue components is fat, constituting up to 40% of all tissues. It is challenging to compare absorption coefficient spectrums of fatty tissues, given the differences between fat and water contents presented throughout the bibliography.

Figure 3.6 represents an assembly of absorption coefficient spectra with corrected data from various research articles compiled by Steven Jacques. This batch includes the work of *van Veen et al.*, which is considered one of the most reliable spectra of the absorption coefficient in fatty tissues available, due to their a priori procedures to the tisssue (careful purification and dehydration). It also includes measurements made in tissues of unknown fat and water content. [5]

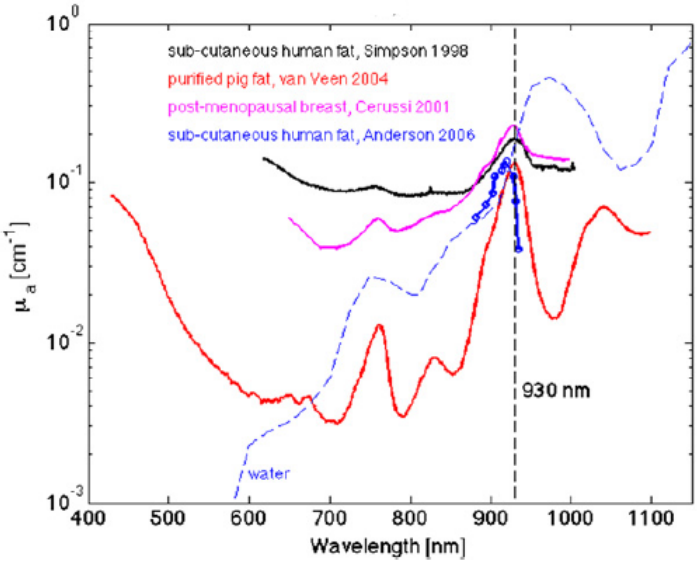

Figure 3.6: Absorption coefficient of fatty tissues versus wavelength [5].

Intralipid (IL), a fat emulsion used clinically as an intravenous nutrient. Due to the fact that is is turbid and a weak absorber in the visible region of the spectrum, is used as a scattering medium for phantoms when conducting optical experiments. The optical properties of Intralipid can not be accurately defined, varying from bottle to bottle. The determination of optical properties of Intralipid by *Flock et al.* was based on measurements on Intralipid 10% with and without an added absorber [10]. The data obtained in the mentioned article is represented in Figure **??**.

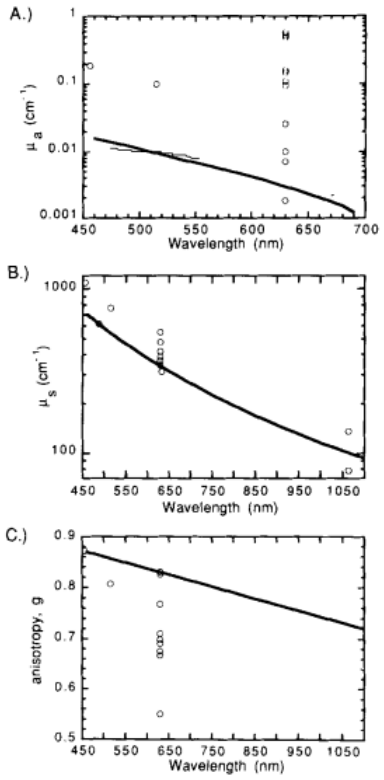

Figure 3.7: Optical properties of solutions with Intralipid 10%: (A) absorption coefficient, (B) scattering coefficient and (C) anisotropy parameter. Data drawn in solid lines were obtained in *Flock et al.* study, and data corresponding to B and C were extrapolated until 1100 nm, from data ranging from 500 to 890 nm and from 460 to 690 nm, respectively [10].

4

Light Propagation Models in Turbid Media

In order to acquire a truthful prediction of the optical properties of a medium, it is essential to model light propagation accurately.
Human tissues can be considered as turbid media, which contain heterogeneous structures that correspond to spatial variations in their optical properties. Multiple scattering events of light are generated by fluctuations in density and optical properties, which then generate a diffuse light field [11].
From an optical perspective, biological tissues can be modeled as systems composed by a homogeneous background medium that englobes randomly distributed scatterers. The referred systems, besides their conceptual simplicity, give a satisfactory description of optical transport in turbid tissues. [11]
Hence, there are two categories which classify light propagation in tissues: particle models and wave models. In the first case, light propagation is described in terms of photon transport, including methods like Radiation Transport Theory (RTT) and Random Walk Model (RWM). On the other hand, the second category resorts to wave propagation theory such as Maxwell equations. [12]

4.1 Radiation Transport Theory

Light propagation through turbid media is described in the RTT model by a fundamental equation, the Radiative Transfer Equation (RTE). This equation regards light as a collection of independently moving particles and expresses the energy balance of this collection of photons present in a volume element of the

medium.

Consider a fixed volume element in which is kept count of incoming, outgoing, absorbed and emitted photons. The previous processes are described by the RTE in terms of intensity of light, but their interference effects are neglected. The propagation of photons per unit area and solid angle is defined as radiance L(r,s,t) - [W/srm^2] :

$$L(r,s,t) = N(r,s,t)\frac{hv}{\lambda} \tag{4.1}$$

where N(s,r,t) is the density per solid angle, h is Plank's constant. N(s,r,t) describes the number of photons at the position r moving at a velocity v in the direction s at a given instant t.

Thus, one approach to express RTE is in terms of the radiance, L, is:

$$\frac{1}{c}\frac{\partial L(r,s,t)}{\partial t} = -s \bigtriangledown L(s,r,t) - (\mu_a + \mu_s)L(s,r,t) + \mu_s \int_{4\pi} L(s,r,t)P(s',s)d\Omega + S(r,s,t) \tag{4.2}$$

The terms on the right hand side of the equation can be interpreted as the flow through the boundaries, loss of energy due to absorption and scattering out of the direction of s, gain of energy through scattering into the direction of s and gain of energy from sources emitting photons located within the volume element, S(r,s,t), respectively. The function P(s',s) is the phase function and represents the probability with light that propagation direction s' being scattered into solid angle $d\Omega$ around s.

Figure 4.1 depicts a representation of photons traveling in the direction s through a volume element V. It is meant to represent the effects of each term of the right hand side of RTE.

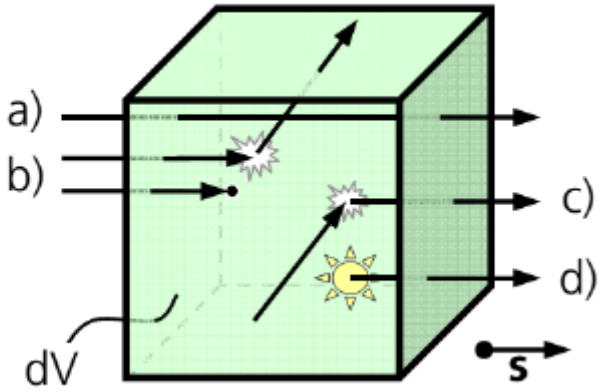

Figure 4.1: Portrayal of the RTE terms. (a) Photons lost through the boundary (radiance). (b) Photons lost due to absorption and scattering out of the direction s. (c) Photon gain by scattering into direction s. (d) Photon gain through sources within the volume dV, from [12].

Equation 4.2 is, however, numerically difficult to solve. Hence, exact solutions cannot be obtained in most situations, and this equation is considered to be too complex to be employed in light propagation analysis in scattering media. Therefore, the use of some approximations is needed to simplify the equation. One of the most commonly used approximations is the Diffusion Approximation (DA), which will be discussed in the following subsection.

4.1.1 Diffusion Approximation

A formal method to solve RTE is to find the solution to its homogeneous part and expand the general solution in terms of the homogeneous solution obtained. In this regard, a simple approach would be to expand the radiance using appropriate function series, as does the diffusion approximation (DA), which expresses the radiance, L, in equation 4.1, in terms of the fluence rate.
The fluence rate, $\Phi(r,t)$ is defined as the energy flow per area moving outward from the volume element at position r and time t:

$$\Phi(r,t) = \int \int L(r,t) d\Omega \tag{4.3}$$

The time-dependent diffusion equation (DE) is often written as:

$$\frac{1}{c}\frac{\partial\Phi(r,t)}{\partial t} = -\mu_a\Phi(r,t) + D \bigtriangledown^2 \Phi(r,t) + S_0(r,t) \tag{4.4}$$

where S(r, t) is the source term, $\Phi(r,t)$ is the fluence rate and D is the diffusion coefficient:

$$D = \frac{1}{3(\mu_a + \mu_s(1-g))} \tag{4.5}$$

This approximation can only be used when the radiance is nearly isotropic and when the point of interest is far from sources or boundaries [13] . This isotropy implies that ($\mu_s' \gg \mu_a$ and that photon propagation distances in media are larger than $\frac{1}{\mu_s'}$, which means that the DE isn't valid in regions close to the light source [12, 14, 15].

Regarding soft tissues, this first condition can, in general, be considered true within the range of 650 - 1300 nm. As for the second condition, it is violated by the calculus of reflectance and transmittance. Nevertheless, it produces accurate estimations of optical properties when the approximation is applied to relative quantities instead of absolute ones.[13]

When applying a short pulse from an isotropic point source, S(r,t)=δ(0,0), it may be shown that, in an infinite medium, the solution to equation 4.4 is:

$$\Phi(r,t) = c(4\pi Dct)^{-3/2} exp\left(\frac{-r^2}{4Dct} - \mu_a ct\right) \tag{4.6}$$

Granted that equation 4.6 is valid in a homogeneous and infinite medium, when implementing the diffusion equation to different circumstances, it is crucial to satisfy boundary conditions [15]. For instance, when considering a semi-infinite medium, one of the boundary conditions to be taken into consideration is the fluence rate at the surface. This condition implies that the fluence rate must be zero at the boundary between media.

In order to ensure a null fluence rate at the surface, as required, a negative source of photons must be added below the boundary, to counteract the effect of the positive source created by the incident light beam. Figure 4.2 illustrates the abovementioned situation and the referred sources [13, 15].

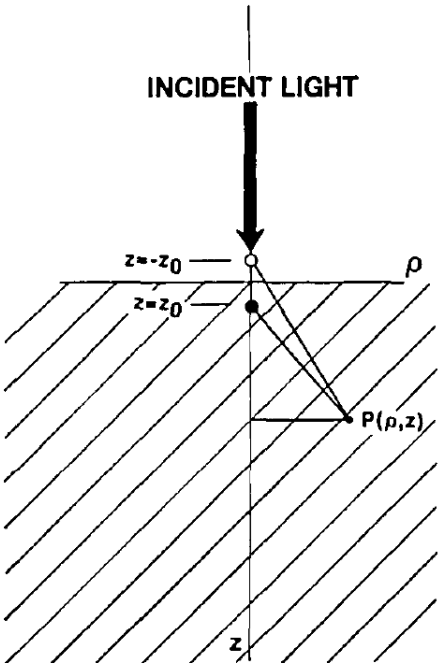

Figure 4.2: Representation of a semi-infinite geometry and the implemented sources to satisfy the discussed boundary condition. The positive and negative sources are positioned at $z = z_0$ and $z = -z_0$, respectively, where $z_0 = \frac{1}{(\mu_s)'}$. This figure was adapted from [13].

By the same token, consider the next simplest case displayed in Figure 4.3: a finite homogeneous slab of thickness d, in which incides a narrow light beam.

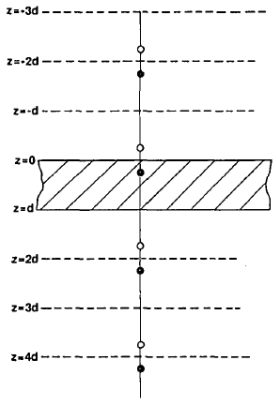

Figure 4.3: Depiction of a homogeneous slab geometry for the calculation of the time resolved transmittance satisfying the boundary conditions for both surfaces. The first four dipole photon sources, and their positioning, are illustrated by open and filled circles (negative and positive, respectively). Figure adapted from [13].

There are now two surfaces to take into account in order to fullfil the boundary conditions. This can be achieved by repeating the process applied in the previous

case. Through the transformation of the source term in the DE into a sum of a series of dipole photon sources located above and below the slab, a null fluence rate at z=0 and z=d is obtained. It is important to highlight that the dipole's contribution decreases with its distance to the first surface.

One approach to positioning these sources is to distribute them simetrically with respect to the first surface illuminated by the beam [15].

4.1.2 Transmittance

Following the development made to DA in the previous section, *Patterson et. al.* presented a model of the time-resolved transmittance through a homogeneous slab as the one represented in Figure 4.3 [13]. This model describes the intensity distribution detected on a surface of a slab of thickness d, when illuminated by a short pulse at a point on the opposite surface.

Hence, the spatially integrated transmitance is given by:

$$T(d,t) = (4\pi D)^{-1/2} t^{-3/2} exp(-\mu_a ct) \times G(d,t) \tag{4.7}$$

Where G(d,t) is the dipole term given by:

$$G(d,t) = \sum_{n=1,k=2n-1}^{n=\infty} \left\{ (kd - z_o) exp\left[\frac{-(d-z_o)^2}{4Dct}\right] - (kd + z_o) exp\left[\frac{-(d-z_o)^2}{4Dct}\right] \right\} \tag{4.8}$$

In order to obtain an analytic expression for transmittance that meets the mentioned boundary conditions and maintains its simplicity, this model retained four dipoles which can be observed in Figure 4.3. Consequently, the transmitted light presents a temporal distribution expressed by:

$$\begin{aligned} T(d,t) = (4\pi D)^{-1/2} t^{-3/2} exp(-\mu_a ct) \times (d - z_o) exp[\frac{-(d-z_o)^2}{4Dct}] - (d + z_o) exp[\frac{-(d-z_o)^2}{4Dct}] \\ + (3d - z_o) exp[\frac{-(d-z_o)^2}{4Dct}] - (3d + z_o) exp[\frac{-(d-z_o)^2}{4Dct}] \end{aligned} \tag{4.9}$$

4.2 Random Walk Models

Another way to describe light propagation through turbid media is to approximate the motion of a photon in such media as a random walk [16]. As the present work was not based on these methods, we display only a brief description of them.

This model is based on certain physical premises: it is assumed that i) the tissue has isotropic properties, ii) Beer's law governs the absorption within the tissue, and iii) photons that have reached the surface contribute to the measured light intensity at said surface.

In random walk models, the description of the behavior of the photon ends when the photon suffers absorption within the tissue or when it reaches the surface of the tissue [16].

If neither of this phenomena occur, the random walk models are able to simulate light propagation by calculating the walk path length of the photon and then calculating its new direction of propagation in media.

The random walk length can be calculated with the formula:

$$L_{rdn} = -ln(\frac{1 - RND}{\mu_t}) \tag{4.10}$$

where RND represents a random number generated between 0 and 1, based on an uniform distribution.

This walk length will be added to the coordinates of the previous location of the photon, in order to obtain its current coordinates (i.e., previously the location of the photon was $[x,y,z]$ and currently is $[x + L_{rdn},y + L_{rdn},z + L_{rdn}]$[17]).

The new direction of propagation of the photon is calculated using the mean cosine of scattering (g) and it depends on its previous direction of propagation.

5

Overview of Time-Resolved studies based on Light Propagation Models

Several methods can be used to estimate the optical properties of tissues. We focused just on time-domain methods using pulsed illumination. A summary review of measurement techniques is given in this section.

- *CosimoD'Andrea et al.* acquired time-resolved images of different liquid phantoms, containing solid inclusions, using a ICCD (Intensified Charged-Coupled Device) based instrumentation. Results were obtained by using a fan geometry (plane matrix of detection points) and fitting experimental data with a mathematical model based on the random walk theory in infinite homogenous slab [18].

- In 1994, *Mitic et al.* resorted to time-gated transillumination to determine the optical parameters of female breast by *in vivo* experiments. The *in vivo* experiments were made after optimizing the time-gated system through systematic phantom experiments. The deduction of both scattering and absorption coefficients is made through the diffusion model, which allows a good modeling of light propagation in turbid media, since the reduced scattering coefficient is greater than 0.5 mm $^{-1}$, for 40 mm thick phantoms [19].

- In order to improve signal-to-noise ratio in acquired data, *Hedben et al.*

describe a method based on a simple diffusion approximation model. This method improves temporal distributions of measurements made with a time-resolved imaging technique. Thus, images of a highly scattering liquid phantom contained in a plastic box with six suspended glass spheres are acquired, and optimized by this method. As opposed to other studies, the main goal is not to accomplish a good prediction of the fitted parametes, but to enhance the obtained curves, considering the theoretical curves "noise free" data [20].

- In 1996, *Cubeddu et al.* used a time-correlated single photon counting (TCSPC) system to obtain measurements on a tissue like phantom. This phantom attempts to replicate a tumor mass within breast tissue, mimicking its optical properties. The acquired transmittance data were fitted with a diffusion model in order to obtain the phantom's optical properties. The tested technique had the ability to detect scattering and absorption inclusions. However, it could only produce good quality images of the scaterring ones [21].

- *Patterson et al.* developed models capable of calculating the pulse shape created either by reflectance or transmittance measurements. These models were established in accordance with the time dependent diffusion equation and demonstrate that factors which describe the pulse shape, such as the instant in which the signal is at its peak, are related to the scattering and absorption coefficients in certain conditions [13].

- *Cubeddu et al.* elaborates a characterization of a solid phantom made of agar, resorting to Intralipid and black ink to emulate optical properties of biological tissues. This homogeneous phantom is characterized through the interpretation of time-resolved transmittance measurements with two theoretical models: random walk theory and diffuse approximation. This paper also proposes and studies different arrangements of inhomogeneous phantoms [22].

- *Madsen et al.* performed experimental tests of the diffusion approximation model in liquid phantoms with different geometries, such as finite slab,

cylindrical and spherical geometries. The best results were provided by a semi-infinite slab geometry. These tests were made through a TCSPC system. [23]

- *Lindquist et al.* proposed a new technique to detect and localize inhomogeneities in turbid media, through interference between diffuse photon density waves. Time-domain measurements were performed by illuminating a tissue phantom, containing inhomogeneities, with two sources, and then analyzing the obtained results in the frequency-domain [24].

- *Pifferi et al.* suggests a method to evaluate optical properties from time-resolved remittance distributions, which yields better results than those obtained from the diffusion approximation [25].

All the referred papers are are listed and compared in Table 5.1:

Table 5.1: A comparison of the presented articles

Author	Time-resolved Remittance	Experimental System	Mathematical Model	Studied Tissue
Cosimo D'Andrea et al. [18]	Transmittance	System based on a gated CCD camera	Random Walk Model	Homogeneous & Inhomoheneous mimicking tissue phantoms
Mitic et al. [19]	Transmittance	System based on a streak camera	Diffuse Approximation Model	Homogeneous mimicking tissue phantoms & *In vivo*
Hebden et al. [20]	Transmittance	System based on a CCD camera coupled to a streak camera	Diffuse Approximation Model	Homogeneous mimicking tissue phantoms with inclusions
Cubeddu et al. [21]	Transmittance	TCSPC System	Diffuse Approximation Model	Homogeneous mimicking tissue phantoms with inclusions
Patterson et al. [13]	Transmittance & Reflectance	System based on a streak camera	Diffuse Approximation Model	*In vivo* measurements
Cubeddu et al. [22]	Transmittance	TCSPC System	Diffuse Approximation Model & Random Walk Model	Homogeneous mimicking tissue phantoms with & without inclusions
Madsen et al. [23]	Reflectance	TCSPC System	Diffuse Approximation Model	Liquid homogeneous mimicking tissue phantoms with & without inclusions
Lindquist et al. [24]	Transmittance & Reflectance	TCSPC System	Diffuse Approximation Model	Liquid homogeneous mimicking tissue phantoms with & without inclusions
Pifferi et al. [25]	Transmittance & Reflectance	TCSPC System	Diffuse Approximation Model & Random Walk Model	Homogeneous mimicking tissue phantoms with & without inclusions

6

Materials and Methods

6.1 Experimental Set-up

The schematic diagram presented in Figure 6.1 describes the time-resolved experimental set-up.

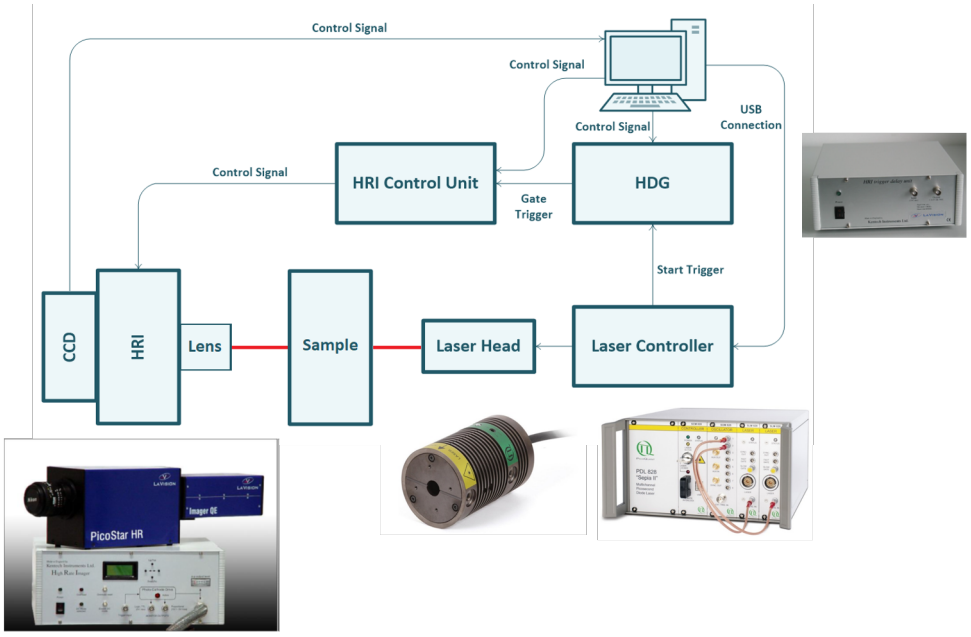

Figure 6.1: Schematic diagram of the implemented time-gated detection system.

The system employs a laser diode head (LDH) (LDH 8-1-971, PicoQuant GmbH, Germany), which produces a beam of light, emitting at 690 nm with a maximum pulsing frequency of 80 MHz. The diode laser head is controlled by a multichannel picosecond diode laser driver (PDL 828 "SEPIA II", PicoQuant GmbH, Germany),

which synchronizes the emission of light pulses with the acquisition system. This synchronization is achieved by the simultaneous emission of a trigger signal to the High Rate Intensifier (HRI) trigger delay unit every time a light pulse is emitted. The light beam delivers short pulses on a tissue-like phantom after traveling through an optical path (see Figure 6.2).

A Lavision ICCD (Intensified Charged-Coupled Device) camera (PicoStar HR, LaVision GmbH, Germany) is implemented as the detector, imaging the output face of the phantom, which is coupled to a Nikon lens (AF NIKKOR 50mm f/1.8D, Nikon, Japan). This camera is based on an HRI, a delay unit (HRI trigger delay unit, Kentech Instruments, UK) and a CCD sensor (Imager Compact, LaVision, Germany).

Even though the used HRI-delay unit is characterized by providing a delay range of 50 ns and a resolution of 1 ps, our measurements had a scan range of approximatelly 1.5 ns. The delay unit output signal then enters the HRI, where the gate-width[1] and gain modulation are controlled. The time-gated detection system records images through a 12-bit CCD, with a resolution of 640 x 480 pixels.

[1]Gate-width is the duration over which the photons are integrated at each time bin [26]

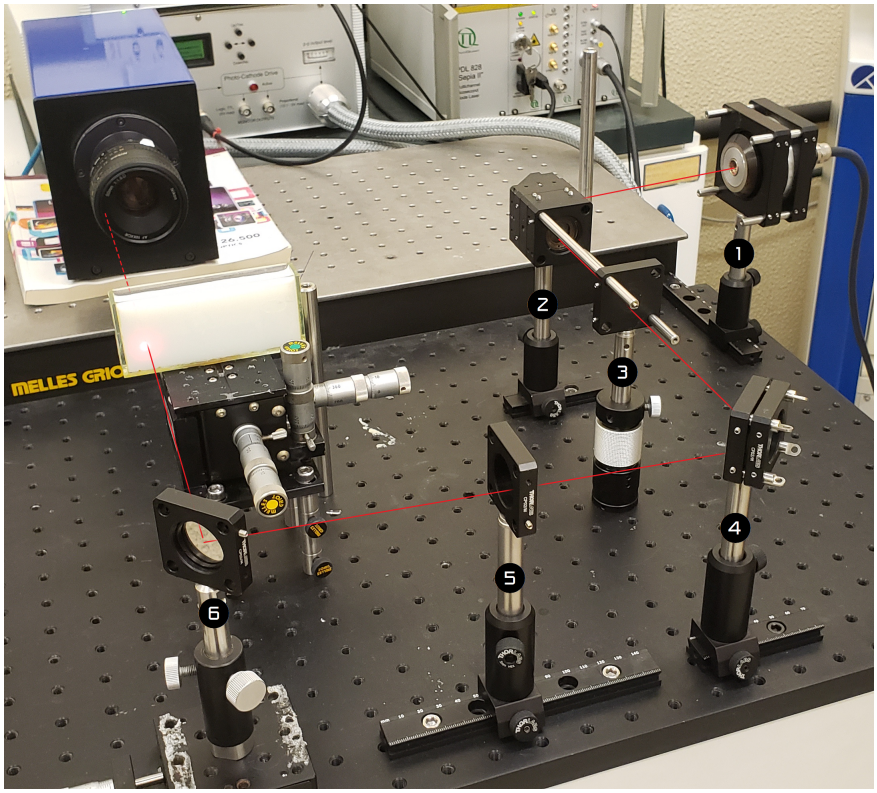

Figure 6.2: Optical path traveled by the laser beam until it reaches the phantom. The beam is emitted by the laser head (1) and is deflected by an optical prism (2). The amount of light that reaches the first mirror (4) is controled by the iris diaphragm (3). The beam incides in the phantom container after passing through a pinhole (5) and a beam spliter mirror (6).

6.2 Phantom Studies

In order to mimic light distributions in biological tissues, it is a common practice to use tissue-simulating optical phantoms [12]. Past studies have used different substances such as milk, Intralipid, coffee, india ink, etc., to produce phantoms with tuned optical properties [27, 28, 22]. The simplest and most usual phantom used for this end is a solution of Intralipid diluted in distilled water. In such solutions, the reduced scattering coefficient can be easily controlled by selecting adequate concentrations of Intralipid [22].

A first set of tests was performed by acquiring images using this liquid phantom contained in a glass rectangular container, with dimensions: 9.7 x 4 x 1.4 cm^3.

However, the use of a container produced artifacts, altering the experimental curves.

Solid phantoms were used instead, to reduce the effect of the used containers in the temporal distributions. After evaluating the different possibilities, the final decision was to design a solid phantom obtained from a 1% agarose solution in distilled water, with the addition of Intralipid to allow the adjustment of the scattering coefficient. Three different types of agar were used.

At an early stage, several phantoms were prepared using comercial agar (Agar agar, Vahiné, France), in order to optimize the dimensions according to the experimental setup requirements (height, thickness, etc.). This first stage yielded satisfatory results, corresponding to the second set of experimental data. However, the durability of the phantoms was limited, lasting only a few days, changing its size over time and, therefore, altering Intralipid and agar concentrations.

Additionally, with the purpose of being able to compare the obtained results with studies already published, and also with the intention of extending the lifetime of the phantoms, it was used a highly purified agar (Agarose A2790, Sigma-Aldrich, USA). However, this specific agar was not adequate for our application, as the phantoms did not hold a vertical position during measurements.

Lastly, another highly purified agar (Agarose A9414, Sigma, USA) with a low melting point was tested. These phantoms were used to acquire the third set of experimental data.

The Agarasose A2790 powder was selected due to its gel strength (500 g/cm^2), which is superior than the A9414 agar gel strength (200 g/cm^2) [29]. However, it yielded more fragile phantoms. The inadequacy of this powder to this specific application can be justified by the interaction of the Intralipid with A2790. There is an easier interaction between Intralipid and the hydroxyl groups available on A9414 than on A2790, which alters the strength of A9414.

The main goal in the production of these phantoms was to ensure that their optical properties were known. For this purpose, each set contained 6 different phantoms, all with the lowest absorption coefficients possible and with different Intralipid concentrations that are presented in Table 6.1.

The method used for the preparation of solid phantoms is described on Subsection

Table 6.1: Phantoms and corresponding Intralipid concentration.

Phantoms	[IL]
1	0.0025
2	0.005
3	0.0075
4	0.01
5	0.0125
6	0.015

6.2.1.

6.2.1 Preparation Procedure of solid phantoms

The preparation of solid phantoms was based on the work of *R.Cubeddu et al* [22], with minor alterations.

Initially, a 1% agar solution was created, by weighing 0,9 g of powder in a precision scale (PFB, Kern, Germany) (Figure 6.3.(a)) and mixing it with 90 ml of distilled water (Figure 6.3.(b)), followed by heating up the solution, under a continuous stir, in a hot plate & stirrer (1000, Jenway, UK), (Figure 6.3.(c)) until it reached 90 ºC. Though the use of a hot plate is unrecommended by *Cubeddu et al* [22], due to the possibility of slightly burning the agar, the temperature was slowly increased, and controlled at all times during the procedure, in order to prevent this from happening.

Once the mixture temperature reached 90 ºC, the solution was stirred in a magnetic stirrer (MR 2000, Heidolph, Germany). The temperature of the solution was measured using the integrated thermometer in a pH meter (3510 pH Meter, Jenway, UK) (Figure6.3.(d)), with the purpose of controlling its decrease until the optimal temperature for mixing the Intralipid 20% (Intralipid 20%, Fresenius Kabi, Portugal) (Figure 6.3.(e)).

When the solution reached the optimal temperature, it was placed into a mould (Figure 6.3.(g)) and, in order to get proper handling and stable optical properties, the mold was not be moved until it cooled down to room temperature. Normally, it would be let to rest from 3 to 5 hours (Figure 6.3.(h)).

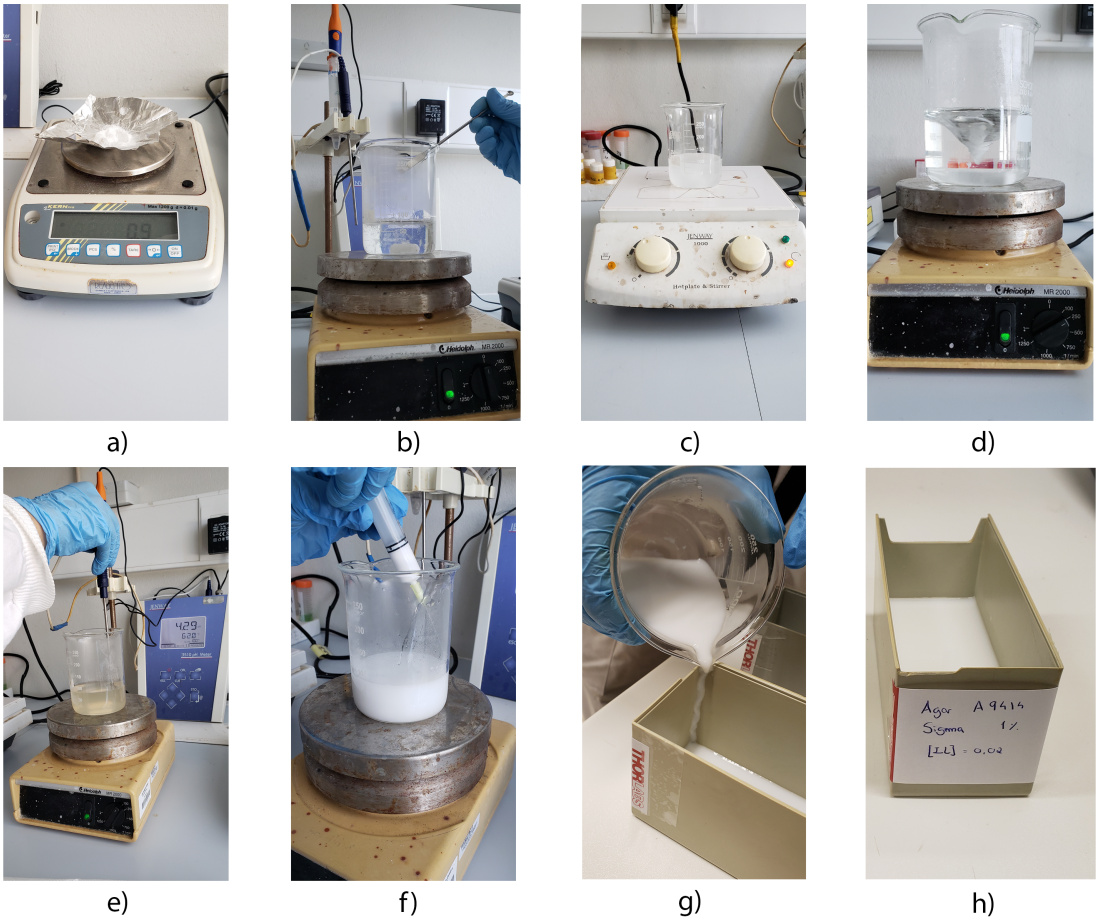

Figure 6.3: Phantom preparation procedure: (a) weighing agar, (b) agar dissolution, (c) heating and stirring the solution, (d) stirring after reaching 90º, (e) temperature control, (f) addition of Intralipid (g) pouring the mixture into the mold, (h) mixture left to rest.

6.2.2 Solid Phantom Design

In order to obtain time-resolved transmittance measurements, the solid phantoms had to be designed according to requirements inherent to the used instrumentation. The established system required the phantom to stand on its own, preventing the appearance of artifacts, constraining its thickness to be at least of 10 mm.

Thicker phantoms require longer exposure times to harness the entire dynamic range of the CCD, implying more time demanding acquisitions. This fact restrained its thickness to a maximum of 15 mm.

The phantom should occupy the field of view of the camera entirely, which is 3.27 x 2.45 cm^2, and be wide enough to be illuminated by the laser outside the field of

view of the camera.

The phantoms were made in a 5.5 x 13.3 x 4.7 cm^3 mold, presented in Figure 6.3(h), which was filled only until it reached the desired thickness. After unmolding (Figure 6.4 (a)) the phantoms were cut (Figure 6.4(b)), endind up with a thickness between 10 and 15 mm, a height of 5.5 cm and a width of aproximately 10 cm.

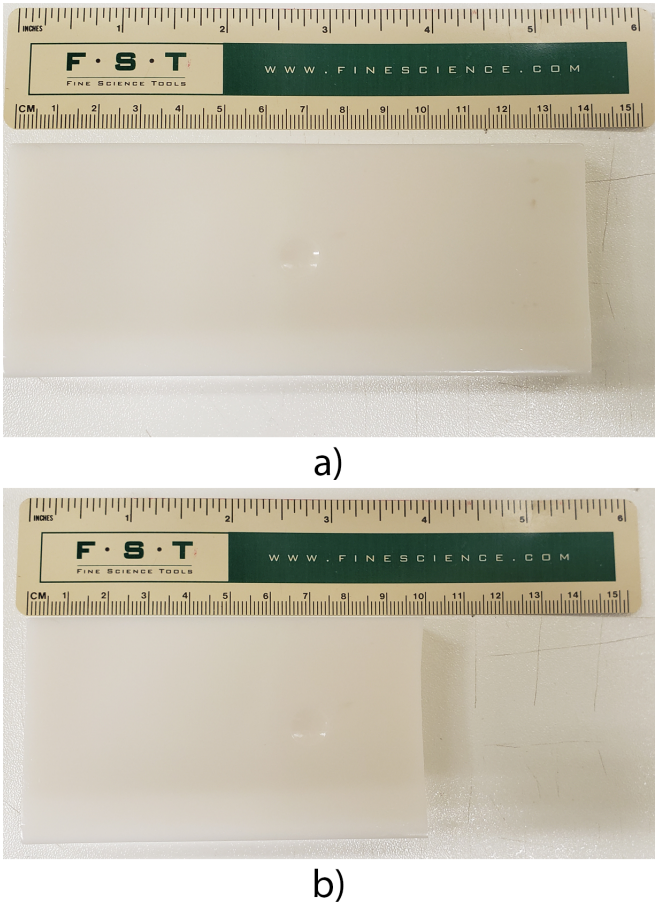

Figure 6.4: Phantom dimensions: after unmolding (a) and after cut (b).

Fulfilling all the requirements mentioned above, the two sets of six solid phantoms were produced.

6.3 Software Description

6.3.1 Data Acquisition

The experimental set-up described before, in Section 6.1, is connected to a computer, which performs device control, data acquisition and storage, through DaVis software (Davis 7.6, LaVision, Germany). This software offers an interface, which controls hardware such as the HRI, the HRI controller, the HRI delay unit and the CCD, as per Figure 6.5. It also provides a 2D imaging tool, which displays measurements in real time, contributing to their optimization.

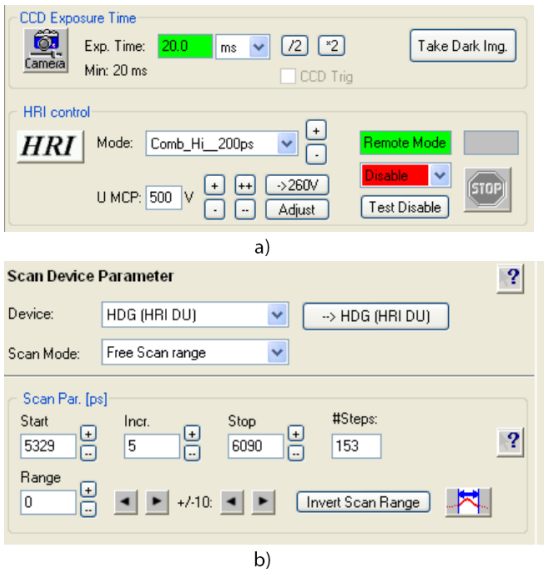

Figure 6.5: Dialog box where the device configuration is made. In (a) the CCD exposure time and the MCP (microchannel plate) voltage are selected, as the HRI mode (which was *Comb_Hi_200ps* for all measurements). In (b) the HRI delay unit is configured by sellecting the best scan parameters. The number of images acquired in each set is dictated by the #Steps, where each image was delayed 6 picoseconds from the previous one.

In this work, the HRI is always operated at Comb_Hi_200ps mode, i.e., a 200 ps gate was shifted across the entire scan range in specific intervals, in order to obtain the number of photons measured at each time bin. The HRI configurations also include setting the gain voltage applied across the microchannel plate (MCP) in the intensifier. The voltage of the MCP was usually set at 500 V, which corresponds to a gain of 1.05 counts per electron that reached the MCP. The exposure time was set

according to the time intensity profile visualized in Davis software, i.e., the selection of the exposure time was made with the intent of using the whole dynamic range (4096 counts) that the CCD provided.

Not all measurements were made with a MCP gain of 500 V due to the long exposure time required by such measurements (around 30 minutes). Instead, the MCP gain was increased to 550/600 V when needed. Although this decision implied a decrease in the S/N ratio, it yielded better results than those obtained with higher exposure times.

Once the acquisition settings were optimized, the measurements were made and stored. Each measurement consisted of a set of images (maximum of 250), and each image stored as an 640 x 480 intensity matrix.

6.3.2 Data Treatment

Data processing started by loading the raw files, produced by Davis software, into MATLAB (The MathWorks Inc., Natick,MA, USA). MATLAB is a programing platform designed for numerical computing, which provides tools for data analysis, algorithm development and creation of models [2].

A set of algorithms was designed to analyze the data matrices extracted from the raw data files. In order to obtain the temporal distribution curves of each measurement, 31 detectors of 20 x 20 pixels were defined in the image plane, as illustrated in Figure 6.6. Each detector collects light exiting from an area corresponding to aproximatelly to 1 x 1 mm^2. Their positioning is aligned with the y-value of the pixel of higher intensity for a given measurement.

[2]https://www.mathworks.com/discovery/what-is-matlab.html

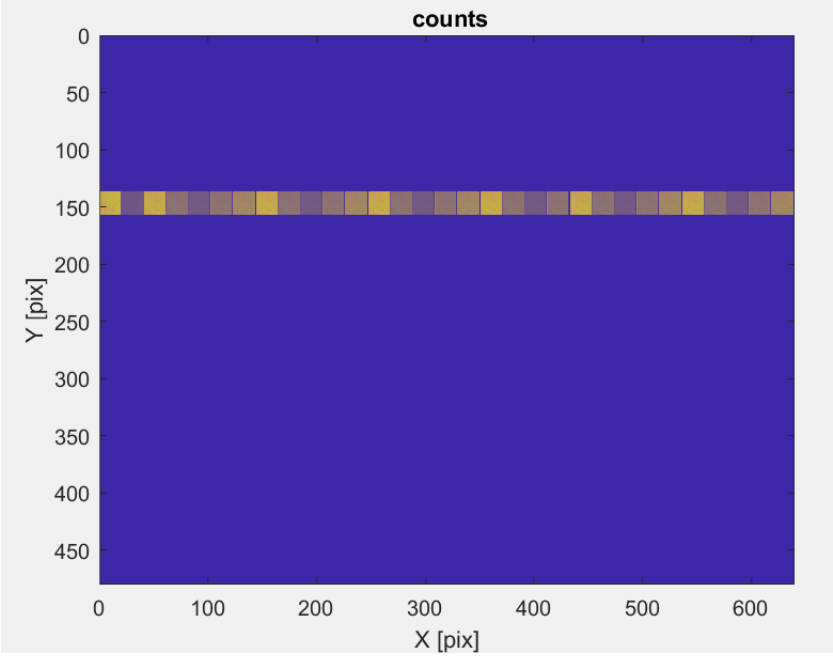

Figure 6.6: Graphic representation of the 31 detectors defined in the image plane. The vertical positioning of the detectors differs from measurement to measurement.

A detector operates like a mask, which was applied to all the images, converting the initial 640 x 480 matrix into a 20 x 20 matrix. This 20 x 20 matrix is then processed in order to obtain a mean value of intensity per image. Each detector produces a temporal distribution curve, its data points correspond to the calculated intensity of each image, as illustrated in Figure 6.7.

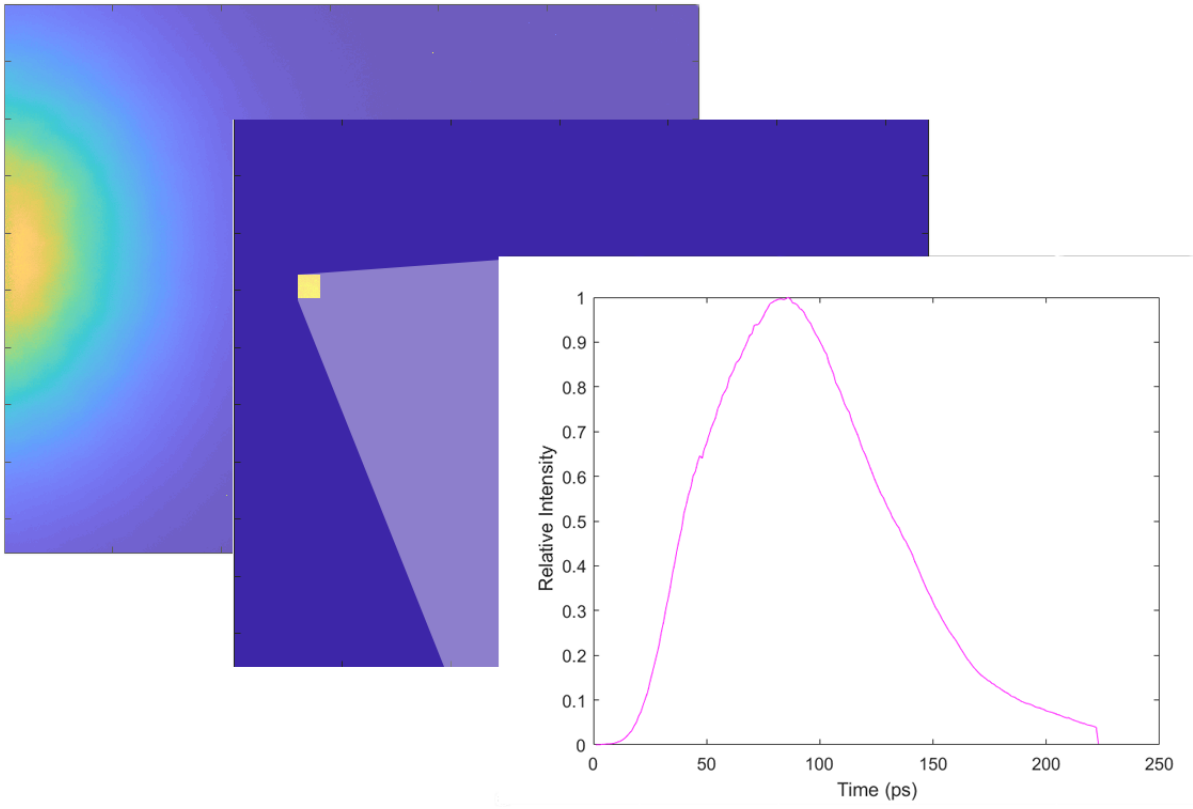

Figure 6.7: Temporal distribution curve produced by a detector defined in the image plane.

Each intensity mean value that was calculated has an associated error that stems from the inherent photon counting statistics and from the instrumentation. These errors were calculated according to the noise model of the experimental system, available in Appendix A.1.

Background correction was implemented by subtracting the darkest image of each measurement from each image of the data volume. In addition to the dark frame subtraction, the temporal curves are normalized. Given the proportionality between the amplitude of the curve and the number of injected photons, this procedure does not affect the results [18]. Finally, only the points with counts higher than 1% of the peak value were considered in the fitting procedure.

6.3.3 Development of a Diffusion Approximation Model

By applying a diffusion approximation model to time-resolved diffuse transmittance, we are able to extract the scattering and absorption coefficients of a homogeneous

medium, as could be seen in section 4.1.2, in Equation 4.9. For the computational implementation of this model, we used Fminuit, a chi-square fitting program, based on the MINUIT minimization engine. Fminuit runs as a Matlab function, giving its user the ability to control the minimization process step by step [3].

Hence, Equation 4.9 had to be written as a Matlab function that depends on two input arguments. The first input argument consisted of a variational parameters vector, μ_a and μ_s. The second one consisted of a 3 column matrix composed by the independent variable (time), measured values of the dependent variable (intensity) and error bars, calculated with the referred noise model. The theoretical curve given by Equation 4.9 is convoluted with the instrument response functions shown in Section 7.1, before Fminuits minimization is applied.

For a better understanding of Fminuit, the following schematic was made:

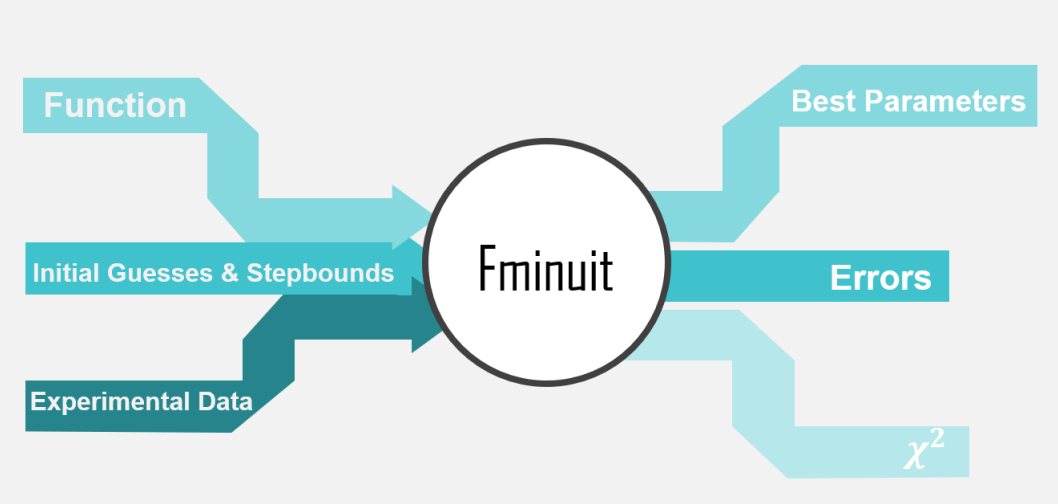

Figure 6.8: Fminuit data flow chart.

To run Fminuit, a few input parameters are needed: a function, initial guesses of the variational parameters of such function (including their limits) and experimental data.

The Matlab routine created with Fminuit is summarized in Figure 6.9. Given the fact that this multidimensional nonlinear minimization allows the user to decide its strategy, (whether the user seeks a fast and less precise minimization or if it agrees

[3] G. Allodi, "FMINUIT - A binding to Minuit for Matlab, Octave Scilab,"2010. - http://www.fis.unipr.it/ giuseppe.allodi/Fminuit/Fminuit_intro.html

with performing a larger number of function calls to obtain the desired precision) the first step was to set a strategy that resulted in a more reliable minimization. Then, a MINOS error analysis was performed, taking into account the problem's non-linearities and the parameter correlations. Although this minimizer requires a more demanding calculation, it provides better results, since it allows the calculation of exact confidence intervals for any parameter. Finally, the minimization of the function is done by the migrad method, a minimization subroutine based on a variable metric method developed by Fletcher [30]. Acording to Minuit Reference Manual, it is the most efficient minimizer. This specific minimizer informs the user when it is not possible to obtain improvements and the routine comes to an end.

At the end of the minimization process, besides returning the optimized parameters and their linearized associated errors, it also calculates the final chi-square value of the fit.

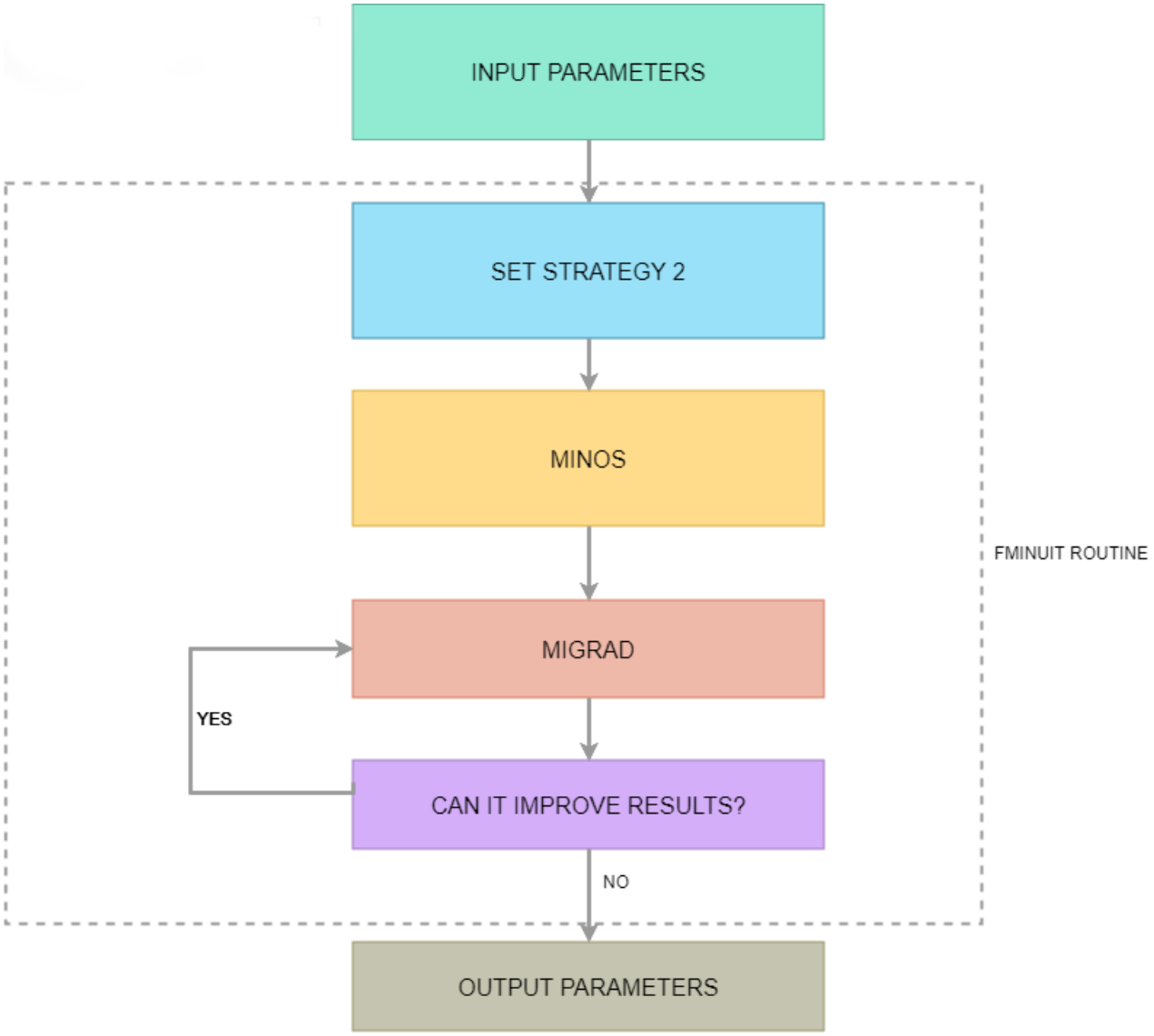

Figure 6.9: A brief description of the executed Fminuit routine. It starts by defining a more reliable strategy, followed by the implementation of two minimizers: Minos and Migrad. The Migrad method is then repeated until it can no longer improve the solutions, ending this routine by displaying the output parameters.

7

Results and Discussion

7.1 System Characterization

Tests were performed with the intent of characterizing the used time-gated system. The following sub-sections describe studies concerning the resolution of the system and the instrument response function.

Image Resolution Test

In order to measure the lateral resolution of our experimental set-up, we used a 1951 USAF (United States Air Force) resolution test target. By imaging a reference line pattern with well-defined dimensions, we were able to measure the pixel size. Hence, a Thorlabs negative target (R3L3S1N Negative 1951 USAF Target, Throrlabs, Germany) (Figure 7.1) was imaged.

The goal of positioning the target on the four quadrants of the field of view (FOV), as depicted in Figure 7.2, was to study the resolution's spatial variation and perform a validation test of the calculated pixel size. The target's patterns are divided into groups identified by numbers as can be seen in Figure 7.1. The pixel size calculation was based on the analysis of the square presented in group -2 and consisted of a mask application on the data matrix, finding out how many pixels were inside the square. Given that the dimensions of said square are tabled, the pixel dimensions were calculated and are presented in Table 7.1.

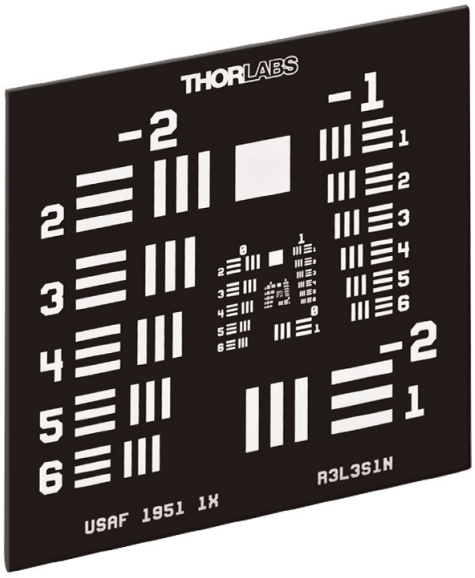

Figure 7.1: Negative USAF target used in the resolution tests. A target designated negative presents low-reflectivity coating to cover the substrates, leaving the patterns clear, performing well in back-lit applications and allowing edge features to be imaged with high resolution (down to approximately 1 μm).

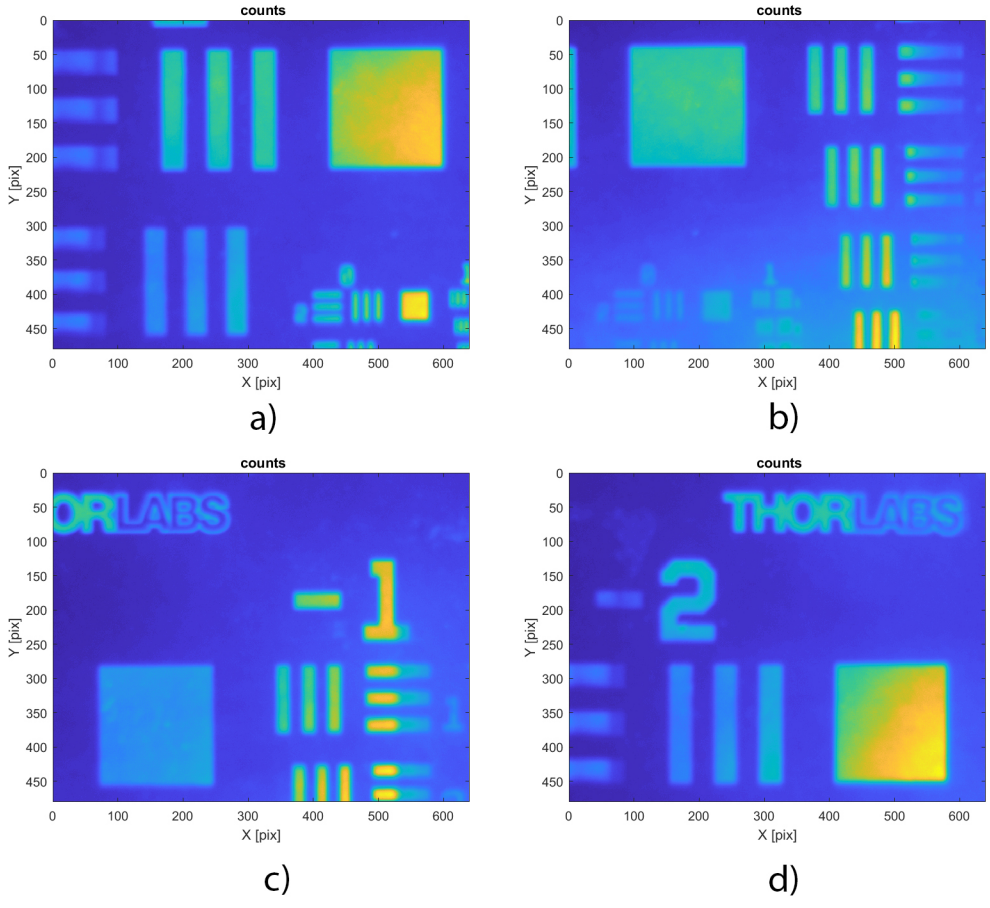

Figure 7.2: Images of the target in four different positions of the FOV.

Table 7.1: Results obtained after performing the 1951 USAF resolution test in all four quadrants of the field of view (FOV).

Image	Pixel Size [x10^{-6} m]	FOV [cm^2]
a)	50.62	3.35 x 2.44
b)	52.12	3.37 x 2.45
c)	50.77	3.25 x 2.44
d)	51.68	3.27 x 2.45

Instrument Response Function Measurement

As covered in Chapter 4, to obtain the optical properties of a phantom, it is necessary to take into account the instrument response function (IRF) of the used experimental set-up. The IRF is given by the pulse shape that the system recorded by the system for a condition of direct incidence of the light beam pulse.

Initially, the measured IRF showed a FWHM (full width at half maximum) of 50.09 ps. However, when imaging liquid phantoms the instrument response function is altered. This change is due to the presence of a glass container and results from secondary reflections on the air-container interfaces. Therefore, when fitting data from liquid phantoms, a different IRF had to be considered. The measurement of a second IRF consisted in imaging the glass box, which would normally contain the liquid phantoms, being illuminated by the light beam. This curve is characterized by a FWHM of 196.68 ps. Figure 7.3 illustrates both measured IRFs.

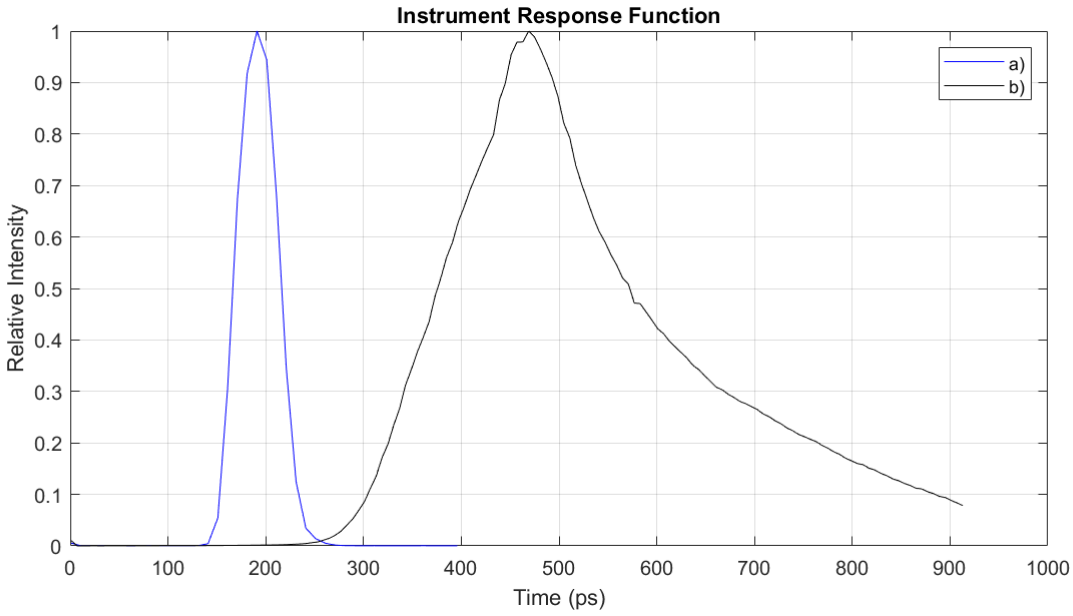

Figure 7.3: Measured Instrument Response Functions: a) IRF obtained by imaging the used light beam with a MCP gain of 260 V, exposure time 20 ms and a delay of 5 ps between images, b) IRF obtained by imaging the container of liquid phantoms illuminated by the light beam with a MCP gain of 260 V, exposure time of 30 ms and a delay of 6 ps between images.

7.2 Methods Validation and Optimization

As we were working with Fminuit for the first time, we had to consider if it was suitable for the intended application and confirm the accuracy of the results. These processes allowed us to evaluate the method's performance and to optimize it, by improving the created routine and its results.

Fit of Synthetic Curves

The first step for method validation used synthetic data curves, generated according to equation 4.9, and analyzed the accuracy and precision of Fminuit in retrieving the optical parameters. The referred set of curves was created by defining both variational parameters, $\mu_s^{'}$ and μ_a, over value ranges that are typical in tissues. This procedure also helped us to assess the influence of optical properties on the transmitted pulse shape.

Since the initial strategy was to study only the variation of the reduced scattering

coefficient, a fixed value of the absorption coefficient was defined to yield the set of synthetic curves presented in Figure 7.4. These curves were treated by Fminuit as an input parameter (as experimental data). The initial guesses of the variational parameters were set equally in all fits to understand how strongly the minimization process relies on these values.

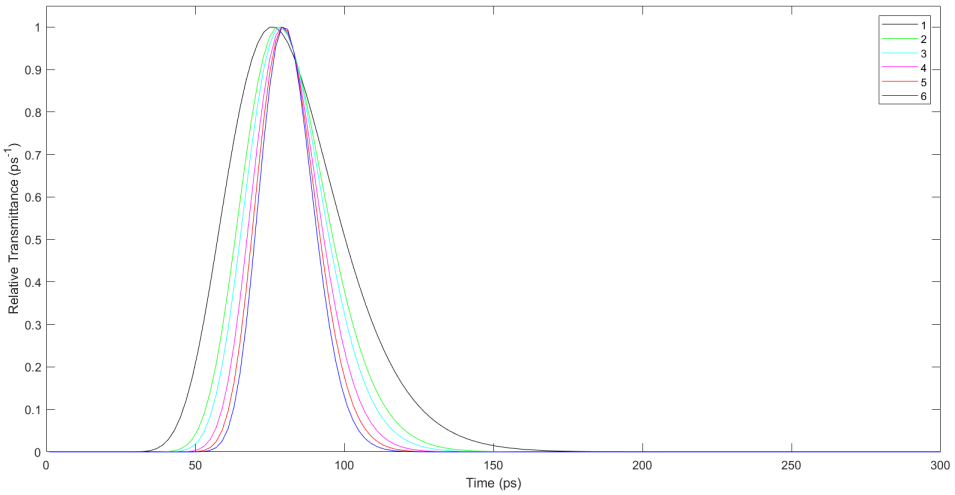

Figure 7.4: Synthetic curves generated according to equation 4.9 by varying their optical parameters. CurveS 1 to 6 were created using the same value for the absorption coefficient and increasing values of the reduced scattering coefficient.

The reduced scattering coefficient used to create the synthetic curves followed the reduced scattering coefficient range found in published studies [18, 22]. These works also used IL to adjust the reduced scattering coefficient of their phantoms. Regarding μ_a, it was set to 0.02 mm^{-1}, which corresponds to an approximated value of the absorption contribution of Intralipid in tissue-like phantoms observed in previous studies [23, 18]. Besides presenting the optical parameters of each curve, Table 7.2 also summarizes the results obtained with the minimization process of each synthetic curve.

We can conclude that Fminuit is capable of adjusting the provided input function until it reaches a condition of convergence, presenting low values of χ^2. From this point on, its assumed that the adjustment of the parameters initial guesses is unnecessary. Thus, the referred values of the initial guesses were used in all minimization processes performed in this study.

Curves	(μ_a,$\mu_s^{'}$)	Initial Guesses	Obtained Parameters	Chi-square
1	(0.02 , 0.5)	(0.004 , 0.8)	(0.0200±0.0113 , 0.5±0.2015)	8.0398e-09
2	(0.02 , 0.9)	(0.004 , 0.8)	(0.0200±0.0266 , 0.9±0.3571)	1.3399e-14
3	(0.02 , 1.1)	(0.004 , 0.8)	(0.0200±0.0213 , 1.1±0.4272)	3.7323e-15
4	(0.02 , 1.5)	(0.004 , 0.8)	(0.0200±0.0329 , 1.5±0.5930)	7.9235e-15
5	(0.02 , 1.9)	(0.004 , 0.8)	(0.0200±0.0281 , 1.9±0.7899)	1.6385e-17
6	(0.02 , 2.3)	(0.004 , 0.8)	(0.0200±0.0311 , 2.3±1.0363)	1.1956e-16

Table 7.2: Fitting parameters obtained by analyzing the created synthetic curves.

Definition of Region of Interest

During the data acquisition, it was made more than one measurement per phantom. After fitting all the obtained data, it could be observed that measurements correspondent to the same phantom, would produce different results. Given this, it was of high importance to establish criteria to choose the most reliable detectors in the most adequate measurement of a certain phantom. To do so, the output parameters of all fits were analysed.

Firstly, a selection of the best measurement of each phantom had to be made. Since the chi-square value evaluates how well the obtained curves of a measurement were described by the DA model, the mean value of χ^2 of each measurement was calculated. The measurement that presented the lowest mean value of chi-square, was selected.

Secondly, to study the behavior of the reduced chi-square value according to the position of the detectors, the values of the reduced chi-square value of each detector of the six different liquid phantoms were summed and displayed in Figure 7.5.

Hence, it was clear that one of the detectors presented better results in the minimization process. Based on this assumption, a 2 cm wide region of interest (ROI) was defined, being centered in the detector positioned at pixel 300. All the results concerning liquid phantoms that will be presented and discussed refer only to the ROI that can be observed in Figure 7.6.

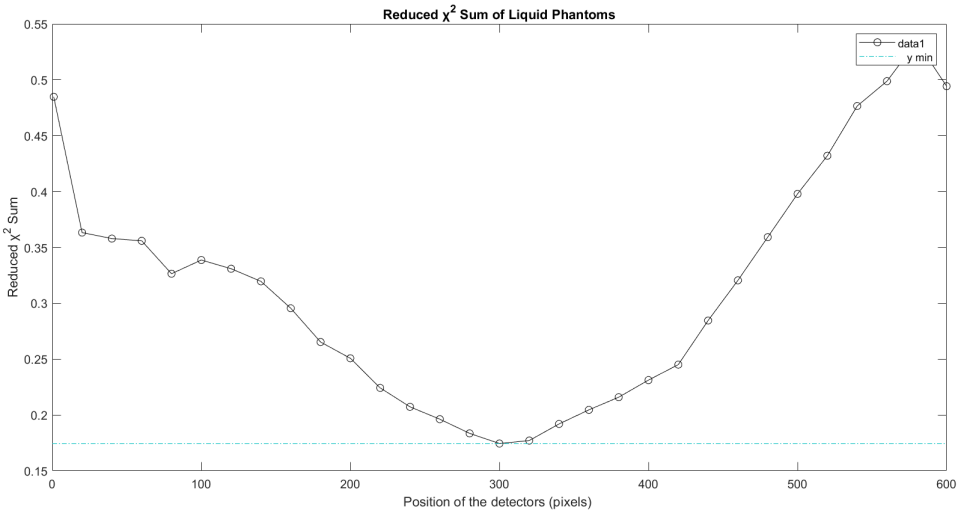

Figure 7.5: Sum of the reduced chi-square value as a function of the positioning of the detectors

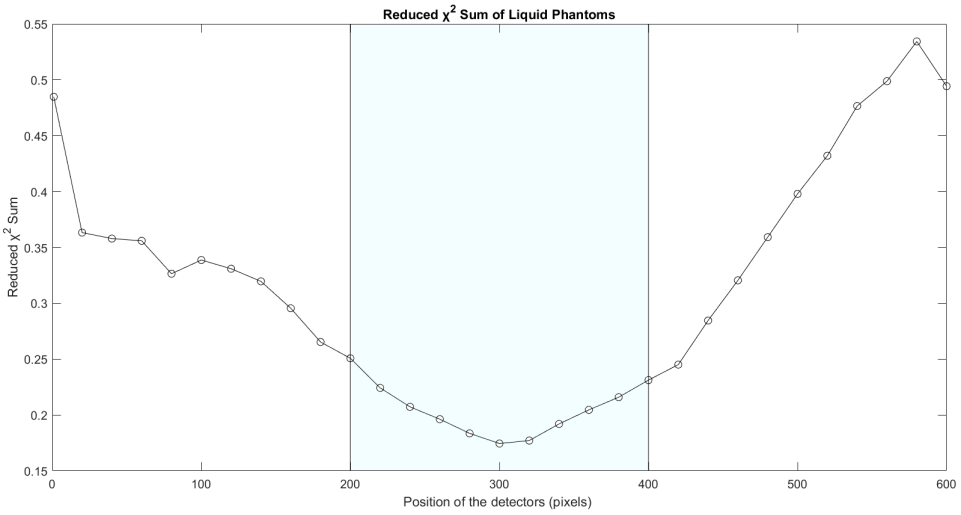

Figure 7.6: Graphic representation of the ROI selected, which englobes 11 detectors placed between pixel 200 and pixel 400.

The same approach was repeated to solid phantoms. The minimum values of the reduced chi-square sum of commercial agar and highly purified agar were obtained for to detectors in pixels 200 and 220, respectively. Given this fact, the ROI chosen to solid phantoms is centered in pixel 200 and 2 cm wide, as presented in Figure 7.7.

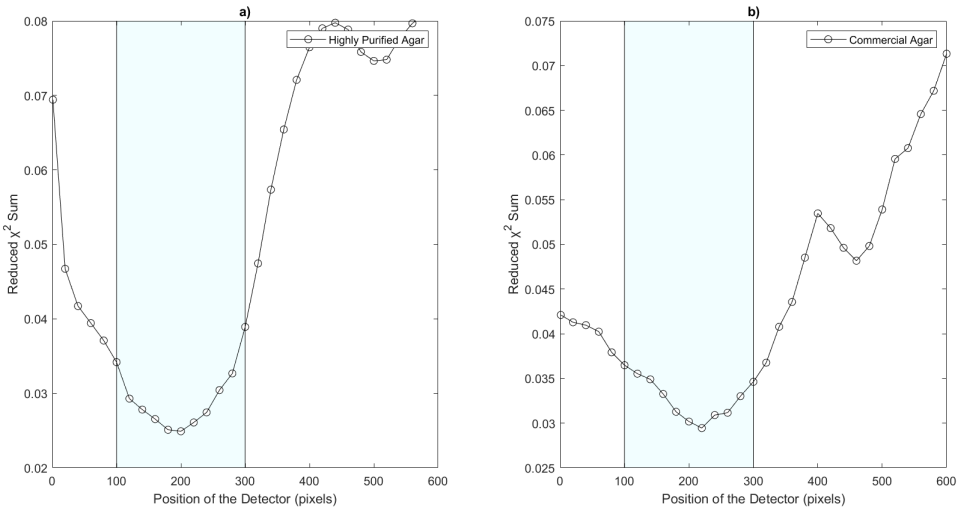

Figure 7.7: Graphic representation of the ROI selected, which englobes 11 detectors placed between pixel 100 and pixel 300.

7.3 Phantom Experimental Results

The measured optical parameters of the imaged phantoms will be presented in this section. The results are organized by the type of phantom, starting by the fitting parameters obtained in the analysis of liquid phatoms measurements and moving on to results for the case of solid phantoms.

- Liquid Phantom Results

The results gathered by fitting the experimental data corresponding to liquid phantoms, are illustrated in Figure 7.8. Within the ROI, it can be observed, as expected, a linear response of the model for reduced scattering coefficients with the IL concentration used in the phantoms. Based on the assumption that IL does not contribute significantly to an increase in the absorption coefficient of a phantom [23], good results were also obtained in what concerns absorption coefficients. Both μ_a and $\mu_s^{'}$ present results within the expected range, by comparision with published studies on similar phantoms [18, 22].

Figure 7.9 shows the results obtained when studying the spatial variation of the optical properties of the liquid phantoms. This figure displays the value of reduced scattering coefficient obtained as a function of the positioning of the detectors

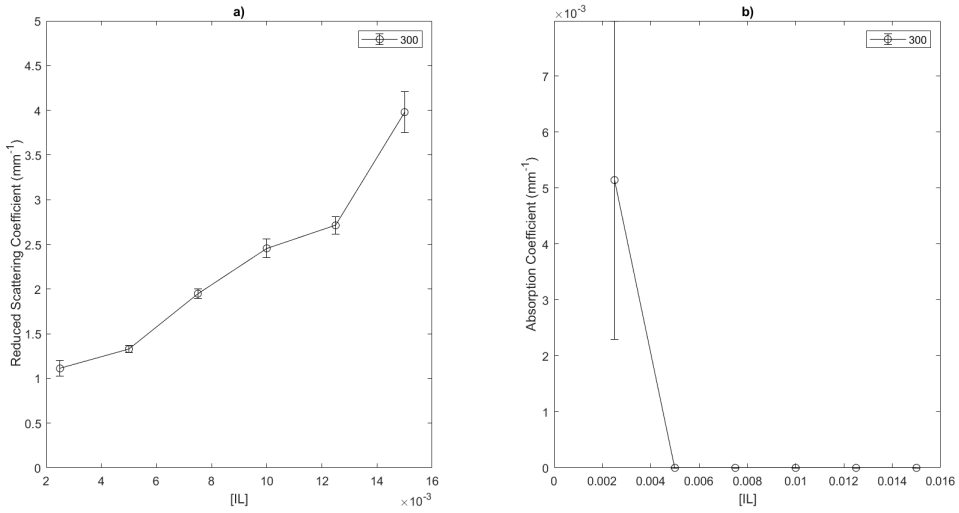

Figure 7.8: Representation of reduced scattering (a)) and absorption (b)) coefficients obtained as functions of the concentration of Intralipid in liquid phantoms.

encountered between pixel 200 and pixel 400.

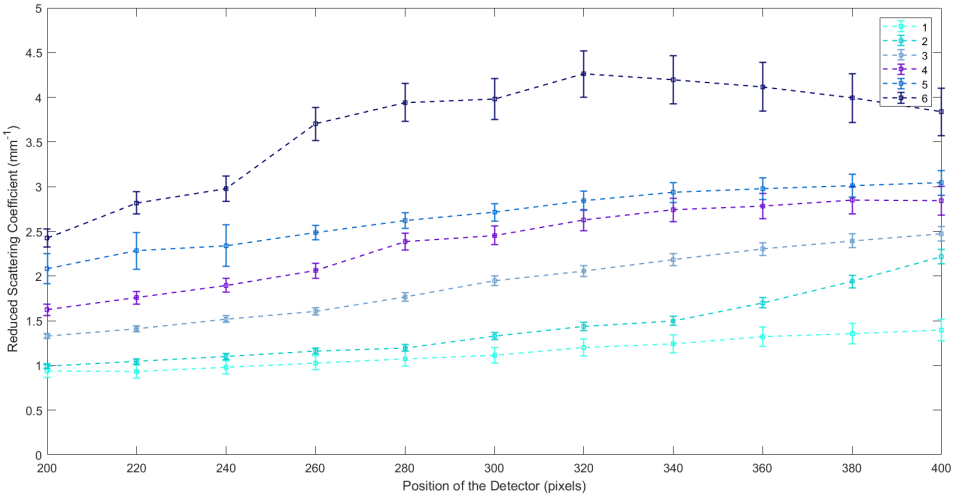

Figure 7.9: Fitting parameters obtained in the analysis of measurements correspondent to liquid phantoms. Results obtained by the 11 detectors enclosed by the selected ROI of a liquid phantom with an IL concentration of: a) 0.0025 b) 0.005, c) 0.0075, d) 0.01, e) 0.0125 and f) 0.015.

Although an increase of $\mu_s^{'}$ is perceived along the horizontal direction, the linear effect of IL concentration on the obtained reduced scattering coefficient is evident.

Regarding absorption coefficients, Figure 7.10(b)), (c)), (d)), and (f)) shows that,

in four out of six liquid phantoms, the obtained absorption coefficient was approximately null.

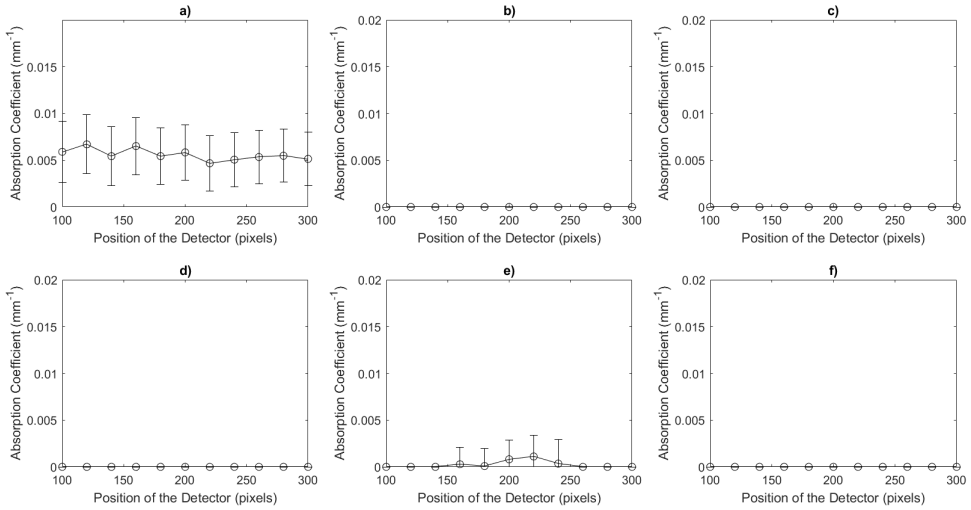

Figure 7.10: Spatial variation of μ_a along the positioning of detectors in the ROI. These results were obtained by imaging a liquid phantom with an IL concentration of: a) 0.0025 b) 0.005, c) 0.0075, d) 0.01, e) 0.0125 and f) 0.015.

Figure 7.10(a)) indicates an absorption coefficient of approximately 0.005 mm^{-1}, which, according to published studies, is a typical value for phantoms that only contain IL [23, 22]. *D'Andrea et al.* detected that an increase in the IL concentration of phantoms led to a slight increase in the absorption coefficient of a phantom [18]. However, *Cubeddu et al.* state that μ_a does not depend on the IL concentration of the phantom [22]. Our results are consistent with the observation made by *Cubbedu's* group, given that, in the case of liquid phantoms, no influence of IL concentration in obtained μ_a was observed, as described in Figure 7.10.

- Solid Phantom Results

Below we present results obtained for solid phantoms made of a commercial agar solution. We observed a similar behavior to that of liquid phantoms.

Comparing Figures 7.8 and 7.11, it can be observed a decrease in the range of values for the obtained reduced scattering coefficients, in the agar phantoms. An agar-related reduction of μ_s' is also referred in a published characterization of similar phantoms [22].

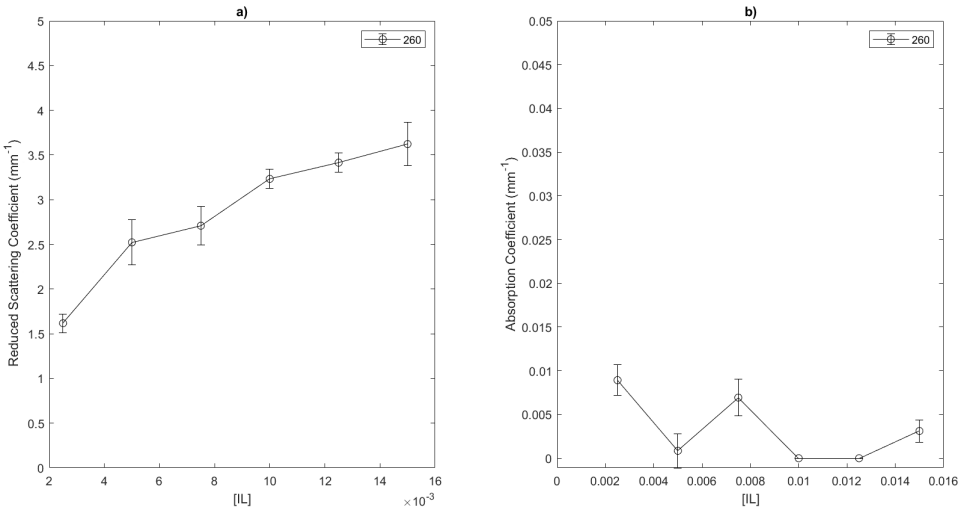

Figure 7.11: Reduced scattering coefficients obtained as a function of the Intralipid concentration in solid phantoms made of commercial agar. Data obtained with detector positioned at pixel 260.

Fitting parameters obtained in the analysis of measurements corresponding to the first set of solid phantoms are depicted in Figure 7.12.

An examination of Figure 7.12, leads us to believe that the preparation procedure of phantoms represented by curves b), d) and e) was not done correctly. These three specific phantoms were produced by adding different amounts of IL to the same agar solution, and their fitting parameters reveal an unexpected behavior along the ROI.

The Matlab code used in the minimization process, was in constant development. Its improvement was tested by analyzing the experimental data of two sets of phantoms (liquid and highly purified solid phantoms). Given this fact, this discrepancy in results corresponding to these kind of phantoms was not detected *a priori*.

However, the cause for these results may be an insufficient mixture of the solution or an occurrence of settling of IL. Although neither of the scientific papers we studied to produce the phantoms, reported these type of problems, this first set of phantoms was made of an agar solution that had not been characterized before.

It is also of importance to highlight that these phantoms were produced in an early phase of this project, when the experience with these procedures was limited.

Figure 7.13 seems to show an increase of μ_a when compared with values obtained for

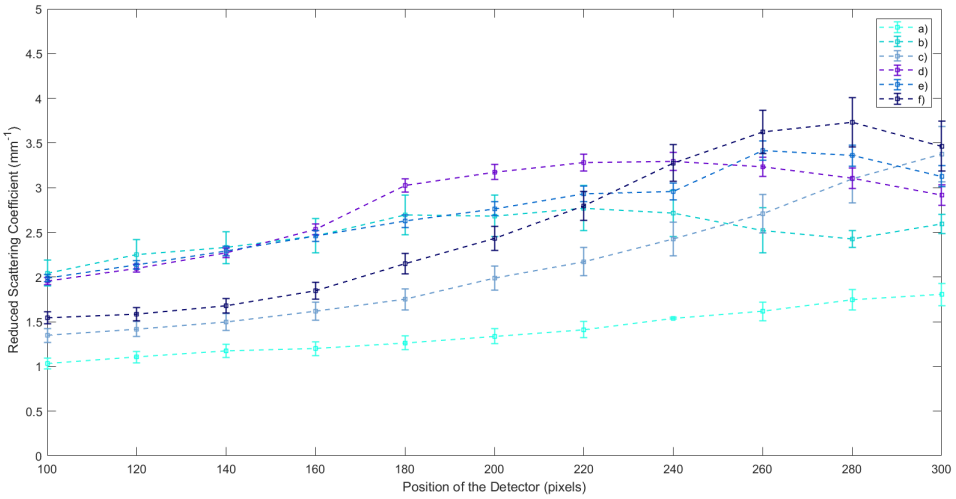

Figure 7.12: Graphic representation of the spatial variation of μ_s' within the defined ROI. Results correspondent to a solid phantom made of commercial agar with an IL concentration of: a) 0.0025 b) 0.005, c) 0.0075, d) 0.01, e) 0.0125 and f) 0.015.

liquid phantoms (Figure 7.10), but since three out of six phantoms did not produced expected fitting parameters, this assumption can not be accurately supported.

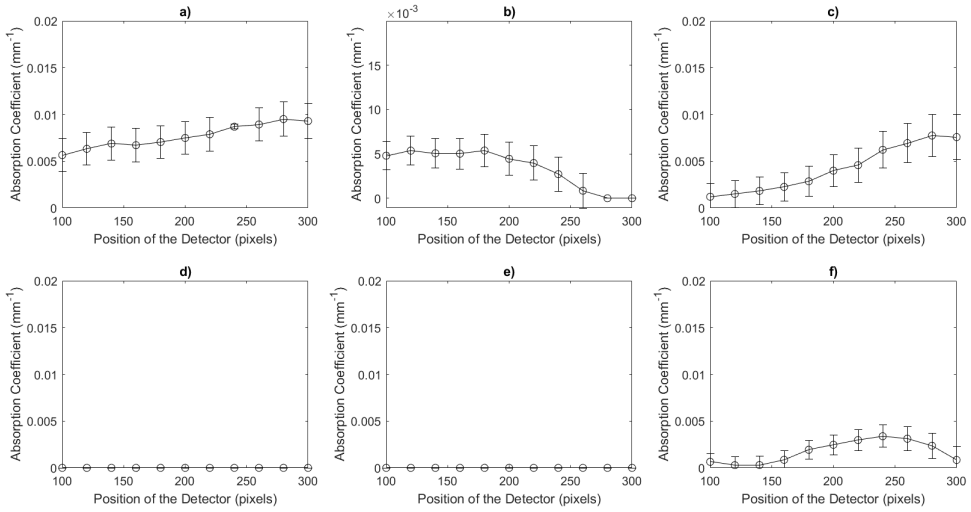

Figure 7.13: Spatial variation of μ_a within the defined ROI. Results correspondent to a solid phantom made of commercial agar with IL concentrations of: a) 0.0025 b) 0.005, c) 0.0075, d) 0.01, e) 0.0125 and f) 0.015.

The results regarding solid phantoms based on a solution of highly purified agar are shown in Figures 7.14 and 7.15. It is also observed a linear relation between

the measured reduced scattering coefficients and the concentration of IL in the phantoms.

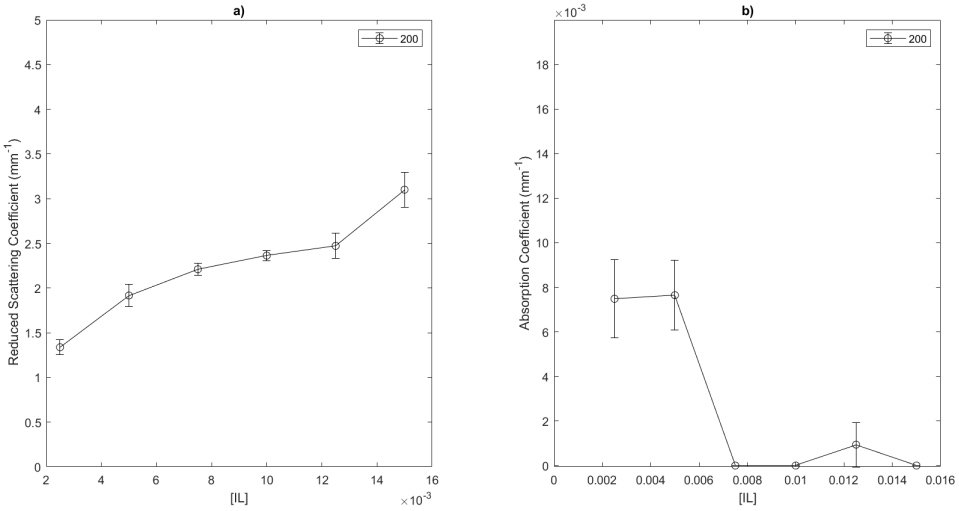

Figure 7.14: Representation of reduced scattering coefficients obtained as a function of the Intralipid concentration in solid phantoms made of a solution of highly purified agar.

Figure 7.15 describes the behaviour of the fitting parameters obtained when the Intralipid concentration of phantom increases. Its analysis reveals a good linearity between $\mu_s^{'}$ and IL concentration. Thus, we can conclude that the preparation procedure allows to adjust the optical properties of the phantom.

For assuring the repeatibility of these phantoms, and in order to guarantee their homogeneity, the preparation procedure should be strickly followed.

Results presented in Figure 7.15 (d)) and (e)) were prepared simultaneously, from the same agar solution. Similarly to what was observed in the case of commercial agar phantoms, these two curves shown an abnormal behavior for detectors positioned to the right of pixel 200.

A more accentuated reduction of the values range of the reduced scattering coefficient was observed, for the same IL concentrations. This agar-related reduction was expected, as both the agar powder used in *Cubeddu*'s work and the agar powder used in this project are supplied by Sigma.

Figure 7.15 describes the behaviour of the fitting parameters obtained when the

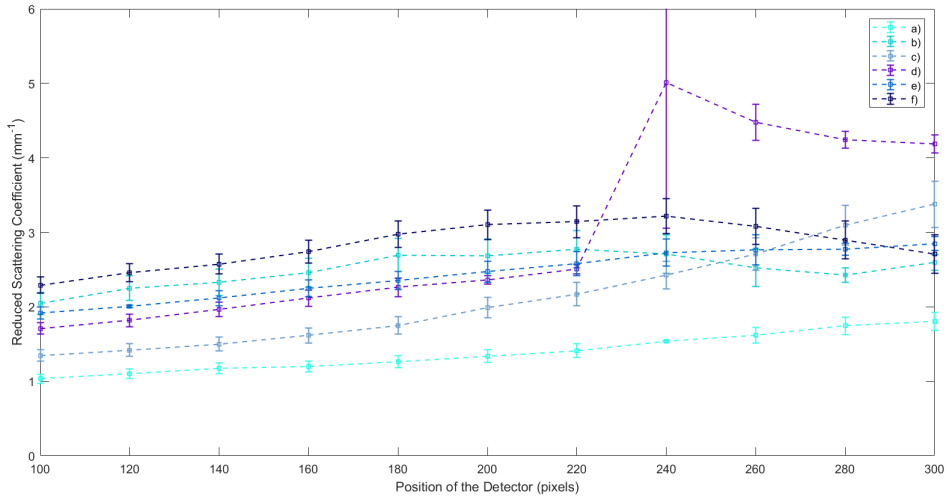

Figure 7.15: Spatial variation of reduced scattering coefficients obtained by the 11 detectors enclosed by the selected ROI of a solid phantom made of an highly purified agar solution with a correspondent IL concentration of: a) 0.0025 b) 0.005, c) 0.0075, d) 0.01, e) 0.0125 and f) 0.015.

Intralipid concentration of phantom increases. Its analysis reveals a good linearity between $\mu_s^{'}$ and IL concentration. Thus, we can conclude that the used phantom preparation procedure provides the capability to adjust the optical properties of a tissue-like phantom. For assuring the repeatibility of these phantoms, and in order to guarantee their homogeneity, the preparation procedure should be strickly followed.

Once again the behavior of the absorption coefficients does not show a dependence with the IL concentration of phantoms, as depicted in Figures 7.14(b) and 7.16.

To conclude this discussion, the information presented in Figures 7.8, 7.11 and 7.14 is merged in Figure 7.17.

From the analysis of this figure, it can be observed that the slope of data correspondent to agarless phantoms is greater than the slope of data correspondent to phantoms that contain agar, confirming the agar-related reduction induced by the presence of agar in phantoms.

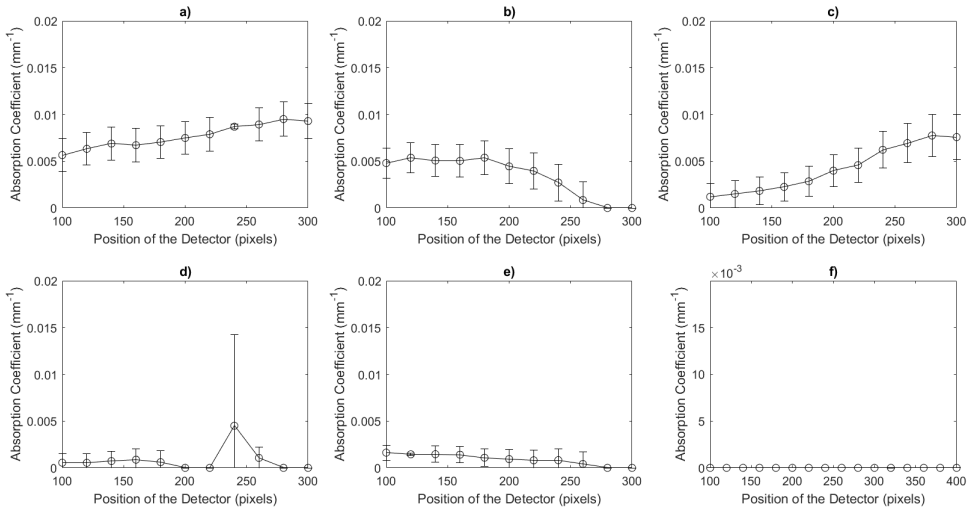

Figure 7.16: Spatial variation of absorption coefficients obtained in the selected ROI of solid phantom made of a highly purified agar solution with an IL concentration of: a) 0.0025 b) 0.005, c) 0.0075, d) 0.01, e) 0.0125 and f) 0.015

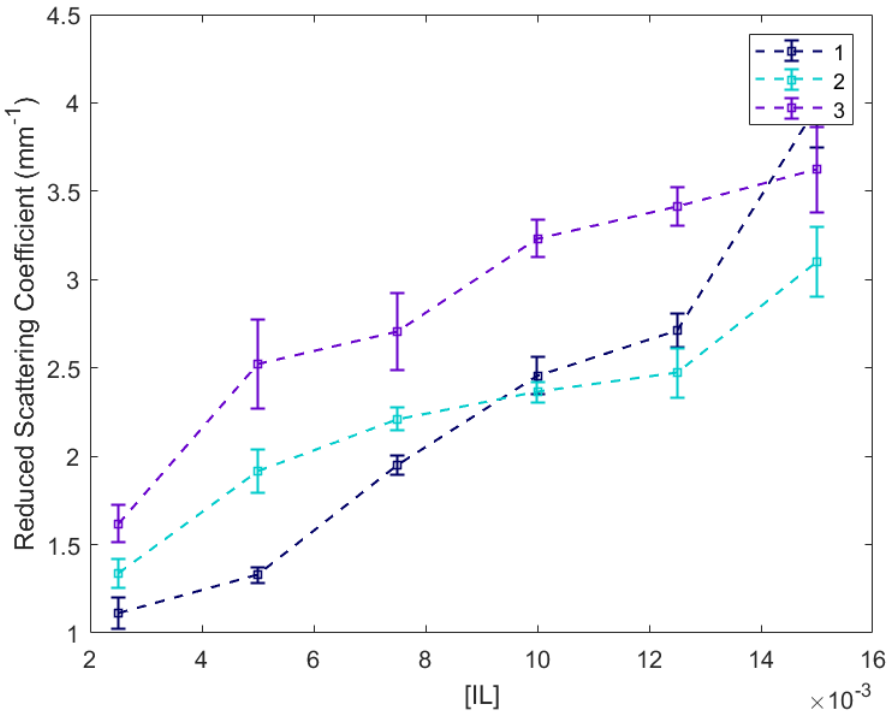

Figure 7.17: The effect of the IL concentration on the reduced scattering coefficients obtained with the developed Diffusion Approximation Model for commercial agar (3), highly purified agar (2) and agarless phantoms (1).

IL was not design for this specific application. Due to inconsistencies in the

manufacturing process of this substance, its optical properties cannot be known without being measured [10]. Hence, it is important to recall that a direct comparison between the presented results and results published concerning equal concentrations of IL cannot be made. All the phantoms were prepared using IL from the same bottle to avoid significant variations of the optical properties of IL in the presented results.

Moreover, reference validation measurements, based on a different technique, were not made. Therefore, we cannot evaluate the accuracy of our measurements, but only infer from the relative behavior of the results from different phantoms.

8

Conclusions and Future Work

8.1 Conclusions

The goal of this thesis ended up being the first step in the development of a technique to measure the optical properties of diffuse media, through the analysis of its time-resolved transmittance measurements, by fitting an analytical function to the time profile of the light pulses at the output interface of the medium.

It was demonstrated that the implemented imaging system is suitable for time-resolved imaging through diffuse media. This instrumentation presents the ability to acquire measurements within a short period of time (maximum of four seconds per image). The developed method allows the adaptation of the data treatment process, being able to alter the detectors positioning and size according to the user's preference. The analysis of the results obtained led us to conclude that:

- According to the obtained chi-square values of the fit, there seems to be a range of detector positions that yielded the best results. It is important to recall that it is not possible to state which was the best detector without the use of a reference technique a scattering standard suitable for transmission measurements.
- It is fundamental to take into account the IRF of the experimental system, especially in experiments conducted in the presence of containers, as per liquid phantoms.
- When using solid phantoms, we measured a reduction of the scattering

coefficients when comparing with equivalent liquid phantoms (i.e. with the same concentration of IL). This agar-related reduction was also reported by other published studies.

- It showed linearity regarding the variation of the reduced scattering coefficient with the concentration of IL in the phantoms, as reported by other authors.

8.2 Future Work

For future work, a key point would be to evaluate the accuracy of this method by using a different technique to measure the optical properties of the samples being imaged or an accepted scattering standard suitable for transmission measurements.

The next logical step would be to infer if the developed method can also show a linear response to an increase of the absorption scattering, as observed in other studies [22, 18]. Eventually, it would be of interest to study the capability of this method to detect inclusions. A further development of this technique may lead to a potential diagnostic tool used for clinical diagnostics and medical imaging.

Bibliography

[1] V. Tuchin, *Tissue Optics, Light Scattering Methods and Instruments for Medical Diagnosis*, vol. 13. 2nd ed., 01 2007.

[2] D. W. Hahn, "Light scattering theory," *Aerospace Engineering*, no. July, pp. 1–13, 2009.

[3] E. Hillman, *Experimental and theoretical investigations of near infrared tomographic imaging methods and clinical applications.* PhD thesis, Univ. London, 2002.

[4] R. Samatham Venkata, *Determination of optical scattering properties of tissues using reflectance-mode confocal microscopy.* PhD thesis, Oregon Health & Science University, 2012.

[5] S. L. Jacques, "Optical properties of biological tissues: a review," *Physics in Medicine and Biology*, vol. 58, pp. R37–R61, May 2013.

[6] V. V. Tuchin, T. Vo-Dinh, and J. Mobley, "Optical Properties of Tissue," in *Biomedical Photonics Handbook: Fundamentals, Devices, and Techniques*, pp. 23–114, CRC Press, 2nd ed., 2015.

[7] F. E. W. Schmidt, *Development of a Time-Resolved Optical Tomography System for Neonatal Brain Imaging.* PhD thesis, University College London, 1999.

[8] S. Prahl, "Optical absorption of hemoglobin." https://omlc.org/spectra/hemoglobin/html, Accessed on 07-Nov-2018.

[9] S. Prahl, "Optical absorption of melanin."

https://omlc.org/spectra/melanin/extcoeff.html, Accessed on 07-Nov-2018.

[10] S. T. Flock, S. L. Jacques, and B. C. Wilson, "Optical Properties of Intralipid : A Phantom Medium for Light Propagation Studies," *Lasers in Surgery and Medicine*, vol. 12, no. 5, pp. 510–519, 1992.

[11] G. Kumar and J. M. Schmitt, "Micro-optical properties of tissue," in *Biomedical Photonics Handbook: Fundamentals, Devices, and Techniques*, CRC Press, 2nd ed., 2015.

[12] M. Sheikhzadeh, "Design , implementation , and evaluation of a fluorescence laminar optical tomography scanner for brain imaging scanner for brain imaging," Master's thesis, University of Wisconsin–Milwaukee, May 2016.

[13] M. S. Patterson, B. Chance, and B. C. Wilson, "Time resolved reflectance and transmittance for the noninvasive measurement of tissue optical properties," *Appl. Opt.*, vol. 28, pp. 2331–2336, jun 1989.

[14] T. Durduran, R. Choe, W. B. Baker, and A. G. Yodh, "Diffuse optics for tissue monitoring and tomography," *Reports On Progress In Physics*, vol. 73 (076701), no. July, 2010.

[15] A. Nordström, "Determination of the optical properties of a paperboard packaging material for laser applications," Master's thesis, Lund Institute of Technology, March 2007.

[16] R. F. Bonner, R. Nossal, and G. H. Weiss, "A random walk theory of time-resolved optical absorption spectroscopy in tissue," in *Photon Migration in Tissues* (B. Chance, ed.), pp. 11–23, Boston, MA: Springer US, 1989.

[17] R. Splinter and B. A. Hooper, *An Introduction to Biomedical Optics*. Optics and Optoelectronics, Bristol, PA, USA: CRC Press, 2006.

[18] C. DAndrea, D. Comelli, A. Pifferi, A. Torricelli, G. Valentini, and R. Cubeddu, "Time-resolved optical imaging through turbid media using a fast data acquisition system based on a gated CCD camera," *Journal of Physics D: Applied Physics*, vol. 36, pp. 1675–1681, jul 2003.

[19] G. Mitic, J. Koelzer, J. Otto, E. Plies, G. Soelkner, and W. Zinth, "Time-gated transillumination of biological tissues and tissuelike phantoms," *Applied optics*, vol. 33, pp. 6699–710, Oct 1994.

[20] J. C. Hebden and D. T. Delpy, "Enhanced time-resolved imaging with a diffusion model of photon transport," *Opt. Lett.*, vol. 19, pp. 311–313, Mar 1994.

[21] R. Cubeddu, A. Pifferi, P. Taroni, A. Torricelli, and G. Valentini, "Time-resolved imaging on a realistic tissue phantom: $\mu s\prime$ and μa images versus time-integrated images," *Appl. Opt.*, vol. 35, pp. 4533–4540, Aug 1996.

[22] R. Cubeddu, A. Pifferi, P. Taroni, A. Torricelli, and G. Valentini, "A solid tissue phantom for photon migration studies," *Phys. Med. Biol.*, vol. 42, no. 10, pp. 1971–1979, 1997.

[23] S. J. Madsen, B. C. Wilson, M. S. Patterson, Y. D. Park, S. L. Jacques, and Y. Hefetz, "Experimental tests of a simple diffusion model for the estimation of scattering and absorption coefficients of turbid media from time-resolved diffuse reflectance measurements," *Appl. Opt.*, vol. 31, pp. 3509–3517, Jun 1992.

[24] C. Lindquist, A. Pifferi, R. Berg, S. andersson engels, and S. Svanberg, "Reconstruction of diffuse photon-density wave interference in turbid media from time-resolved transmittance measurements," *Applied Physics Letters*, vol. 69, pp. 1674–1676, 09 1996.

[25] A. Pifferi, P. Taroni, G. Valentini, and S. andersson engels, "Real-time method for fitting time-resolved reflectance and transmittance measurements with a monte carlo model," *Applied optics*, vol. 37, pp. 2774–80, 05 1998.

[26] V. Venugopal, J. Chen, and X. Intes, "Development of an optical imaging platform for functional imaging of small animals using wide-field excitation," *Biomedical Optics Express*, vol. 1, no. 1, pp. 512–516, 2010.

[27] S. A. Burgess, *Development and Applications of Laminar Optical Tomography for In Vivo Imaging.* PhD thesis, Columbia University, 2011.

[28] B. W. Pogue and M. S. Patterson, "Review of tissue simulating phantoms for

optical spectroscopy, imaging and dosimetry," *Journal of Biomedical Optics*, vol. 11, no. 4, pp. 1 – 16, 2006.

[29] "Agarose selection." https://www.sigmaaldrich.com/life-science/biochemicals/agarose/agarose-selection.html, Accessed on 14-Aug-2019.

[30] R. Fletcher, "A new approach to variable metric algorithms," *The Computer Journal*, vol. 13, pp. 317–322, 01 1970.

Appendices

A

Appendix A

A.1 Noise Model

When calculating the detected noise signal in the used ICCD imaging system, it is important to take into account the different types of noise. Thus, intensity values have associated errors that stem from inherent photon counting statistics, which can be described by the following equation:

$$\sigma_I^2 = k^2 E N_{ph} + \sigma_k^2 N_{ph}^2 + \sigma_{CCD}^2 \tag{A.1}$$

Where k represents the camera gain, i.e., the counts detected by the CCD per electron that reached the MCP, E represents the excess noise factor, N_{ph} represents the number of detected photons, corresponding to the number of counts in each pixel, σ_k^2 is the noise associated with camera gain fluctuations and σ_{CCD}^2 represents the readout noise (equivalent to 2.28 counts). Considering σ_k^2 null we end up with:

$$\sigma_I^2 = k^2 E N_{ph} + \sigma_{CCD}^2 \tag{A.2}$$

Equation A.2 was used to calculate the noise associated with pixels intensity value according to the MPC gain applied in each measurement and correspondent k and E values that are presented in Table A.1:

Table A.1: Reference values for the excess noise factor and camera gain according to the UMCP applied.

E	UMPC(V)	k
	260	0,01
	300	0,02
	350	0,06
	400	0,17
	450	0,43
2,203	500	1,05
1,842	550	2,41
1,653	600	5,2
1,461	650	11,1
1,315	700	21,6
1,158	750	45